A hybrid mimetic spectral element method for three-dimensional linear elasticity problems

Zhang, Yi; Fisser, Joël; Gerritsma, Marc

DOI
10.1016/j.jcp.2021.110179

Publication date
2021

Document Version
Final published version

Published in
Journal of Computational Physics

Journal of Computational Physics 433 (2021) 110179

Contents lists available at ScienceDirect

Journal of Computational Physics

www.elsevier.com/locate/jcp

A hybrid mimetic spectral element method for three-dimensional linear elasticity problems

Yi Zhang *, Joël Fisser, Marc Gerritsma

Delft University of Technology, Faculty of Aerospace Engineering, Kluyverweg 1, 2629 HS Delft, the Netherlands

ARTICLE INFO

Article history:
Available online 4 February 2021

Keywords:
Mimetic spectral element method
Hybridization
Domain decomposition
Variational principle
Lagrange multiplier
De Rham complex

ABSTRACT

We introduce a domain decomposition structure-preserving method based on a hybrid mimetic spectral element method for three-dimensional linear elasticity problems in curvilinear conforming structured meshes. The method is an equilibrium method which satisfies pointwise equilibrium of forces. The domain decomposition is established through hybridization which first allows for an inter-element normal stress discontinuity and then enforces the normal stress continuity using a Lagrange multiplier which turns out to be the displacement in the trace space. Dual basis functions are employed to simplify the discretization and to obtain a higher sparsity. Numerical tests supporting the method are presented.

1. Introduction

Structure-preserving or *mimetic methods* are numerical methods that aim to preserve fundamental properties of the continuous problems, like conservation laws (for example equilibrium of forces in elasticity), at the discrete level. The mimetic spectral element method (MSEM) [1] is a novel arbitrary order mimetic method that usually uses the mixed formulation. It has been applied to, for instance, Stokes flow [2], the Poisson equation [3], the Grad-Shafranov equation [4], the shallow water equations [5], and, recently, linear elasticity [6]. The mixed formulation, together with high order methods, generally leads to large and dense matrices. This is particularly the case when one considers the three-dimensional mixed elasticity formulation which solves for three physical quantities, namely displacement, rotation and stress, simultaneously in a global discrete system. Displacement and rotation fields consist of three components while the stress tensor field has nine components. This makes the MSEM an expensive method for three-dimensional linear elasticity. An effective way to overcome this drawback is to use the hybrid finite element method [7,8], a domain decomposition method which breaks up the problem into smaller sub-problems.

Within the world of mimetic methods we distinguish between various numerical methods. A particular branch of these methods is the mimetic finite difference methods, see [9] and its references. The virtual element method [10,11] is another way in which mimetic ideas are represented. In yet another branch the mathematical language of differential forms and similarities between differential forms and algebraic topology is exploited, [12,13]. A pioneering work of implementing these ideas in numerical analysis was first conducted by Bossavit [14] in computational electromagnetism. Later, a common framework of using differential forms and algebraic topology for mimetic discretizations was developed by Bochev and Hyman [15]. Some important contributions in the context of finite element discretizations were then made by Arnold, Falk

* Corresponding author.
E-mail address: zhangyi_aero@hotmail.com (Y. Zhang).

https://doi.org/10.1016/j.jcp.2021.110179

and Winther, [16,17]. The extension to spectral element methods is given by the MSEM. Initially, the MSEM was introduced using the mathematical language of differential forms, which is preferable but less popular than conventional vector/tensor calculus for the mathematical description of physics [18]. It is possible to translate the mathematical language of differential forms into vector/tensor calculus to reach a larger audience. The work in, e.g., [4,6] and the present paper are examples.

In solid mechanics, finite element methods are developed based on variational principles. In classic finite element methods, stiffness matrices representing the variational principle in elements are established and assembled. Elements are then coupled in the global stiffness matrix through the strong inter-element continuity. Unlike classic finite element methods, hybrid finite element methods first allow for an inter-element discontinuity and then impose the continuity with the help of a Lagrange multiplier [7]. This process is usually called *hybridization*. The first hybrid finite element method, the assumed stress hybrid method [19], was proposed by Pian in the 1960s. Other hybrid finite element methods in solid mechanics are, for example, the assumed displacement hybrid method [20] and the assumed stress-displacement hybrid mixed method [21]. The advantage of the addition of the extra continuity equation with the associated Lagrange multiplier is that it may be possible to solve for the interface Lagrange multiplier first, after which the global system decouples into independent problems at element level. This is particularly efficient for spectral element methods where the number of interface unknowns is relatively small compared to the global number of unknowns. The mortar element method [22–24], a domain decomposition method which couples different non-overlapping subdomains uses a similar idea. The idea of hybridization also plays an important role in the finite element tearing and interconnecting (FETI) method [25,26]. For linear elasticity, one of the main problems in hybrid finite element methods is the appearance of so-called *spurious kinematic modes* or *zero energy modes*, see, for instance, [27–29]. These spurious modes consist of non-solid body deformations which do not affect the stress field indicating that such hybrid formulations are non-wellposed. In [30], the well-posedness of problems arising from the hybrid variational principles and the error behavior of the hybrid method are studied. Hybridizing certain existing mixed finite element methods is studied in [31].

In this work, we introduce a hybrid mimetic spectral element method (hMSEM) based on a new hybrid variational principle for three-dimensional linear elasticity problems. The method is an arbitrary order structure-preserving method which satisfies pointwise equilibrium of forces and, to our knowledge, is the first method that manages to reduce the computational cost of the MSEM without the introduction of spurious kinematic modes. Besides the computational cost reduction as a result of the hybridization, additional reduction is obtained through the use of dual basis functions [32–34] which significantly increases the sparsity of the discrete system. Dual basis functions can also be applied to the original, non-hybrid, MSEM to improve its efficiency.

The layout of the paper is as follows: In Section 2, a brief introduction to the three-dimensional linear elasticity problem is given, which is followed by an introduction of a hybrid mixed formulation and its weak formulation in Section 3. The proposed method is then explained in detail in Section 4. Numerical experiments are presented in Section 5. Finally, conclusions are drawn in Section 6.

2. Three-dimensional linear elasticity

In $\mathbb{R}^3$ with coordinate system $\{x, y, z\}$, let $\boldsymbol{u} = \begin{Bmatrix} u_x & u_y & u_z \end{Bmatrix}^\mathsf{T}$ be the displacement vector. The rotation vector $\boldsymbol{\omega}$ is given by

$$\boldsymbol{\omega} = \begin{Bmatrix} \omega_x \\ \omega_y \\ \omega_z \end{Bmatrix} = \frac{1}{2} \begin{Bmatrix} 0 & -\partial/\partial z & \partial/\partial y \\ \partial/\partial z & 0 & -\partial/\partial x \\ -\partial/\partial y & \partial/\partial x & 0 \end{Bmatrix} \begin{Bmatrix} u_x \\ u_y \\ u_z \end{Bmatrix}. \tag{1}$$

We use D to represent the divergence matrix,

$$D = \begin{Bmatrix} \partial/\partial x & \partial/\partial y & \partial/\partial z & 0 & 0 & 0 & 0 & 0 & 0 \\ 0 & 0 & 0 & \partial/\partial x & \partial/\partial y & \partial/\partial z & 0 & 0 & 0 \\ 0 & 0 & 0 & 0 & 0 & 0 & \partial/\partial x & \partial/\partial y & \partial/\partial z \end{Bmatrix}.$$

Its transpose, D^T, then is the gradient matrix. The strain vector $\boldsymbol{\varepsilon} = \begin{Bmatrix} \varepsilon_{xx} & \varepsilon_{yx} & \varepsilon_{zx} & \varepsilon_{xy} & \varepsilon_{yy} & \varepsilon_{zy} & \varepsilon_{xz} & \varepsilon_{yz} & \varepsilon_{zz} \end{Bmatrix}^\mathsf{T}$ can be written as $\boldsymbol{\varepsilon} = D^\mathsf{T}\boldsymbol{u} + R^\mathsf{T}\boldsymbol{\omega}$, where R is a matrix given by

$$R = \begin{Bmatrix} 0 & 0 & 0 & 0 & 0 & 1 & 0 & -1 & 0 \\ 0 & 0 & -1 & 0 & 0 & 0 & 1 & 0 & 0 \\ 0 & 1 & 0 & -1 & 0 & 0 & 0 & 0 & 0 \end{Bmatrix}.$$

The stress vector $\boldsymbol{\sigma} = \begin{Bmatrix} \sigma_{xx} & \sigma_{yx} & \sigma_{zx} & \sigma_{xy} & \sigma_{yy} & \sigma_{zy} & \sigma_{xz} & \sigma_{yz} & \sigma_{zz} \end{Bmatrix}^\mathsf{T}$ can be computed using the constitutive relation, $\boldsymbol{\sigma} = C^{-1}\boldsymbol{\varepsilon}$, where C, given by

$$C = \frac{1}{E}\begin{Bmatrix} 1 & 0 & 0 & 0 & -\nu & 0 & 0 & 0 & -\nu \\ 0 & 1+\nu & 0 & 0 & 0 & 0 & 0 & 0 & 0 \\ 0 & 0 & 1+\nu & 0 & 0 & 0 & 0 & 0 & 0 \\ 0 & 0 & 0 & 1+\nu & 0 & 0 & 0 & 0 & 0 \\ -\nu & 0 & 0 & 0 & 1 & 0 & 0 & 0 & -\nu \\ 0 & 0 & 0 & 0 & 0 & 1+\nu & 0 & 0 & 0 \\ 0 & 0 & 0 & 0 & 0 & 0 & 1+\nu & 0 & 0 \\ 0 & 0 & 0 & 0 & 0 & 0 & 0 & 1+\nu & 0 \\ -\nu & 0 & 0 & 0 & -\nu & 0 & 0 & 0 & 1 \end{Bmatrix},$$

is the compliance tensor. E and ν represent Young's modulus and Poisson's ratio of the material, respectively. Equilibrium of forces states that $D\boldsymbol{\sigma} + \boldsymbol{f} = 0$, where $\boldsymbol{f} = \begin{Bmatrix} f_x & f_y & f_z \end{Bmatrix}^{\mathsf{T}}$ is the body force vector, and equilibrium of moments implies $R\boldsymbol{\sigma} = 0$. If we put the stress components in a 3 by 3 tensor, equilibrium of moments then implies that the stress tensor is symmetric.

We now consider a bounded, connected domain Ω with boundary $\partial\Omega = \Gamma_{\boldsymbol{u}} \cup \Gamma_{\boldsymbol{t}}$, where $\Gamma_{\boldsymbol{u}} \cap \Gamma_{\boldsymbol{t}} = \emptyset$, $\Gamma_{\boldsymbol{u}} \neq \emptyset$. On $\Gamma_{\boldsymbol{u}}$, the displacement $\boldsymbol{u}$ is prescribed; $\boldsymbol{u}|_{\Gamma_{\boldsymbol{u}}} = \widehat{\boldsymbol{u}} = \begin{Bmatrix} \widehat{u}_x & \widehat{u}_y & \widehat{u}_z \end{Bmatrix}^{\mathsf{T}}$. On $\Gamma_{\boldsymbol{t}}$, the surface traction $\boldsymbol{t}$ is prescribed; $\boldsymbol{t}|_{\Gamma_{\boldsymbol{t}}} = \widehat{\boldsymbol{t}} = \begin{Bmatrix} \widehat{t}_x & \widehat{t}_y & \widehat{t}_z \end{Bmatrix}^{\mathsf{T}}$. The three-dimensional linear elasticity problem then can be formulated as

$$C\boldsymbol{\sigma} - D^{\mathsf{T}}\boldsymbol{u} - R^{\mathsf{T}}\boldsymbol{\omega} = 0 \quad \text{in } \Omega, \tag{2a}$$

$$D\boldsymbol{\sigma} + \boldsymbol{f} = 0 \quad \text{in } \Omega, \tag{2b}$$

$$-R\boldsymbol{\sigma} = 0 \quad \text{in } \Omega, \tag{2c}$$

$$\boldsymbol{u} = \widehat{\boldsymbol{u}} \quad \text{on } \Gamma_{\boldsymbol{u}}, \tag{2d}$$

$$\boldsymbol{t} = N\boldsymbol{\sigma} = \widehat{\boldsymbol{t}} \quad \text{on } \Gamma_{\boldsymbol{t}}, \tag{2e}$$

where the body force $\boldsymbol{f}$ is known, and N is a matrix given by

$$N = \begin{Bmatrix} n_x & n_y & n_z & 0 & 0 & 0 & 0 & 0 & 0 \\ 0 & 0 & 0 & n_x & n_y & n_z & 0 & 0 & 0 \\ 0 & 0 & 0 & 0 & 0 & 0 & n_x & n_y & n_z \end{Bmatrix},$$

where n_x, n_y, n_z are components of the unit outward normal vector, $\boldsymbol{n} = \begin{Bmatrix} n_x & n_y & n_z \end{Bmatrix}^{\mathsf{T}}$. It is straightforward to prove that the solutions $\boldsymbol{u}$ and $\boldsymbol{\omega}$ of problem (2) satisfy relation (1).

3. A hybrid mixed formulation

3.1. Notations

Throughout the paper, we restrict ourselves to the Hilbert spaces $L^2(\Omega)$, $H^1(\Omega)$, $H(\mathrm{div};\Omega)$, trace spaces $H^{1/2}(\partial\Omega)$ and $\left(H^{1/2}(\partial\Omega)\right)'$ [35], and their extensions to $[\cdot]^3$ in $\mathbb{R}^3$. The dual spaces are expressed with the notation $(\cdot)'$. For example,

$$\left(H^{1/2}(\partial\Omega)\right)' = H^{-1/2}(\partial\Omega).$$

The subspace $H_0(\mathrm{div};\Omega;\Gamma)$ is defined as

$$H_0(\mathrm{div};\Omega;\Gamma) := \{\boldsymbol{\varphi} \,|\, \boldsymbol{\varphi} \in H(\mathrm{div};\Omega),\ \mathrm{tr}\boldsymbol{\varphi} = N\boldsymbol{\varphi} = \boldsymbol{0} \text{ on } \Gamma\}.$$

Without loss of generality, in this section, we will assume the Neumann boundary condition to be $\widehat{\boldsymbol{t}}|_{\Gamma_{\boldsymbol{t}}} = \boldsymbol{0}$.

3.2. A mixed formulation

Given $\boldsymbol{f} \in \left[L^2(\Omega)\right]^3$ and $\widehat{\boldsymbol{u}} \in \left[H^{1/2}(\Gamma_{\boldsymbol{u}})\right]^3$, for $(\boldsymbol{\sigma},\boldsymbol{u},\boldsymbol{\omega}) \in [H_0(\mathrm{div};\Omega;\Gamma_{\boldsymbol{t}})]^3 \times \left[L^2(\Omega)\right]^3 \times \left[L^2(\Omega)\right]^3$, a variational formulation based on the principle of minimizing the complementary energy, (i), subject to constraints of equilibrium of forces, (ii), and equilibrium of moments, (iii), is written as, [6],

$$\mathcal{L}(\boldsymbol{\sigma},\boldsymbol{u},\boldsymbol{\omega};\boldsymbol{f},\widehat{\boldsymbol{u}}) = \underbrace{\frac{1}{2}(\boldsymbol{\sigma},C\boldsymbol{\sigma})_\Omega - \langle\widehat{\boldsymbol{u}},\boldsymbol{t}\rangle_{\Gamma_{\boldsymbol{u}}}}_{\text{(i)}} + \underbrace{(\boldsymbol{u},D\boldsymbol{\sigma}+\boldsymbol{f})_\Omega}_{\text{(ii)}} - \underbrace{(\boldsymbol{\omega},R\boldsymbol{\sigma})_\Omega}_{\text{(iii)}}, \tag{3}$$

where $(\cdot,\cdot)_\Omega$ denotes the L^2-inner product and the duality pairing, $\langle\cdot,\cdot\rangle_{\Gamma_{\boldsymbol{u}}}$, between $\widehat{\boldsymbol{u}} \in \left[H^{1/2}(\Gamma_{\boldsymbol{u}})\right]^3$ and $\boldsymbol{t} = \mathrm{tr}\boldsymbol{\sigma} \in \left[\left(H^{1/2}(\Gamma_{\boldsymbol{u}})\right)'\right]^3$ stands for a boundary integral. Its stationary points weakly solve the problem (2), and the corresponding mixed weak formulation is: Given $\boldsymbol{f} \in \left[L^2(\Omega)\right]^3$ and $\widehat{\boldsymbol{u}} \in \left[H^{1/2}(\Gamma_{\boldsymbol{u}})\right]^3$, find $(\boldsymbol{\sigma},\boldsymbol{u},\boldsymbol{\omega}) \in [H_0(\mathrm{div};\Omega;\Gamma_{\boldsymbol{t}})]^3 \times \left[L^2(\Omega)\right]^3 \times \left[L^2(\Omega)\right]^3$ such that

$$\left(\overline{\boldsymbol{\sigma}}, C\boldsymbol{\sigma}\right)_\Omega + \left(\boldsymbol{u}, D\overline{\boldsymbol{\sigma}}\right)_\Omega - \left(\boldsymbol{\omega}, R\overline{\boldsymbol{\sigma}}\right)_\Omega = \left\langle\widehat{\boldsymbol{u}}, \overline{\boldsymbol{t}}\right\rangle_{\Gamma_{\boldsymbol{u}}}, \qquad \forall\, \overline{\boldsymbol{\sigma}} \in [H_0(\mathrm{div};\Omega;\Gamma_{\boldsymbol{t}})]^3, \tag{4a}$$

$$\left(\overline{\boldsymbol{u}}, D\boldsymbol{\sigma}\right)_\Omega = -\left(\overline{\boldsymbol{u}}, \boldsymbol{f}\right)_\Omega, \quad \forall\, \overline{\boldsymbol{u}} \in \left[L^2(\Omega)\right]^3, \tag{4b}$$

$$-\left(\overline{\boldsymbol{\omega}}, R\boldsymbol{\sigma}\right)_\Omega = 0, \qquad \forall\, \overline{\boldsymbol{\omega}} \in \left[L^2(\Omega)\right]^3. \tag{4c}$$

3.3. The hybrid formulation

To construct a hybrid mixed formulation, we first let a mesh, denoted by Ω^h, partition the domain Ω into M disjoint subdomains, Ω_m, $m = 1, 2, \cdots, M$, and use Γ_{ij} to denote the interface between subdomains Ω_i and Ω_j.

Given $\boldsymbol{f} \in \left[L^2(\Omega_m)\right]^3$ and $\widehat{\boldsymbol{u}} \in \left[H^{1/2}(\partial\Omega_m \cap \Gamma_{\boldsymbol{u}})\right]^3$, for $(\boldsymbol{\sigma},\boldsymbol{u},\boldsymbol{\omega},\boldsymbol{\lambda}) \in [H_0(\mathrm{div};\Omega_m;\partial\Omega_m\cap\Gamma_{\boldsymbol{t}})]^3 \times \left[L^2(\Omega_m)\right]^3 \times \left[L^2(\Omega_m)\right]^3 \times \left[H^{1/2}(\Gamma_{ij})\right]^3$, a hybrid variational formulation is expressed as

$$\mathcal{L}(\boldsymbol{\sigma},\boldsymbol{u},\boldsymbol{\omega};\boldsymbol{f},\widehat{\boldsymbol{u}}) = \sum_m \left[\frac{1}{2}\left(\boldsymbol{\sigma}, C\boldsymbol{\sigma}\right)_{\Omega_m} - \left\langle\widehat{\boldsymbol{u}}, \boldsymbol{t}\right\rangle_{\partial\Omega_m\cap\Gamma_{\boldsymbol{u}}} + \left(\boldsymbol{u}, D\boldsymbol{\sigma} + \boldsymbol{f}\right)_{\Omega_m} - \left(\boldsymbol{\omega}, R\boldsymbol{\sigma}\right)_{\Omega_m}\right] - \sum_{ij}\left\langle\boldsymbol{\lambda}, \boldsymbol{t}_i + \boldsymbol{t}_j\right\rangle_{\Gamma_{ij}}, \tag{5}$$

where $\boldsymbol{t}_i$ and $\boldsymbol{t}_j$ are surface tractions of subdomains Ω_i and Ω_j ($\overline{\Omega}_i \cap \overline{\Omega}_j \neq \emptyset$), i.e., $\boldsymbol{t}_i = N_i\boldsymbol{\sigma}_i$, $\boldsymbol{t}_j = N_j\boldsymbol{\sigma}_j$, and, on Γ_{ij}, $N_i = -N_j$. Across the interface of subdomains, the surface tractions $\boldsymbol{t}_i$ and $\boldsymbol{t}_j$ can differ from each other. To enforce the continuity, we introduce the Lagrange multiplier $\boldsymbol{\lambda} \in \left[H^{1/2}(\Gamma_{ij})\right]^3$ and add the surface integral constraint to the variational formulation. If we perform variational analysis of (5) with respect to $\boldsymbol{\sigma}$ in a particular subdomain, for example, the subdomain Ω_m who is a neighbor of subdomains Ω_n ($\Gamma_{mn} \neq \emptyset$), we have

$$\left(\overline{\boldsymbol{\sigma}}, C\boldsymbol{\sigma}\right)_{\Omega_m} - \left\langle\widehat{\boldsymbol{u}}, \overline{\boldsymbol{t}}\right\rangle_{\partial\Omega_m\cap\Gamma_{\boldsymbol{u}}} + \left(\boldsymbol{u}, D\overline{\boldsymbol{\sigma}}\right)_{\Omega_m} - \left(\boldsymbol{\omega}, R\overline{\boldsymbol{\sigma}}\right)_{\Omega_m} - \sum_n \left\langle\boldsymbol{\lambda}, \overline{\boldsymbol{t}}\right\rangle_{\Gamma_{mn}} = 0.$$

If the solution is sufficiently smooth, we can perform integration by parts to the third term,

$$\left(\boldsymbol{u}, D\overline{\boldsymbol{\sigma}}\right)_{\Omega_m} = -\left(D^{\mathsf{T}}\boldsymbol{u}, \overline{\boldsymbol{\sigma}}\right)_{\Omega_m} + \left\langle\boldsymbol{u}, \overline{\boldsymbol{t}}\right\rangle_{\partial\Omega_m},$$

and use the fact $\left(\boldsymbol{\omega}, R\overline{\boldsymbol{\sigma}}\right)_{\Omega_m} = \left(\overline{\boldsymbol{\sigma}}, R^{\mathsf{T}}\boldsymbol{\omega}\right)_{\Omega_m}$, we would obtain

$$\left(\overline{\boldsymbol{\sigma}}, C\boldsymbol{\sigma} - D^{\mathsf{T}}\boldsymbol{u} - R^{\mathsf{T}}\boldsymbol{\omega}\right)_{\Omega_m} + \left\langle\boldsymbol{u} - \widehat{\boldsymbol{u}}, \overline{\boldsymbol{t}}\right\rangle_{\partial\Omega_m\cap\Gamma_{\boldsymbol{u}}} + \sum_n \left\langle\boldsymbol{u} - \boldsymbol{\lambda}, \overline{\boldsymbol{t}}\right\rangle_{\Gamma_{mn}} = 0, \quad \forall\, \overline{\boldsymbol{\sigma}} \in [H_0(\mathrm{div};\Omega_m;\partial\Omega_m\cap\Gamma_{\boldsymbol{t}})]^3.$$

This implies

$$C\boldsymbol{\sigma} - D^{\mathsf{T}}\boldsymbol{u} - R^{\mathsf{T}}\boldsymbol{\omega} = 0 \quad \text{in } \Omega_m,$$

and

$$\boldsymbol{u} = \widehat{\boldsymbol{u}} \quad \text{on } \partial\Omega_m \cap \Gamma_{\boldsymbol{u}},$$
$$\boldsymbol{u} = \boldsymbol{\lambda} \quad \text{on } \partial\Omega_m \setminus \partial\Omega.$$

So the Lagrange multiplier that enforces the continuity across the subdomains has a physical interpretation; it represents the displacement along the interface. Similar discussions about that the Lagrange multiplier in the trace space of the hybrid method has a physical meaning can be found in [31]. If we perform variational analysis with respect to $\boldsymbol{\sigma}$, $\boldsymbol{u}$, and $\boldsymbol{\omega}$ in all subdomains Ω_m and with respect to $\boldsymbol{\lambda}$ on all interfaces Γ_{ij}, we will find that the stationary points of (5) weakly solves the following problem,

$$C\boldsymbol{\sigma} - D^{\mathsf{T}}\boldsymbol{u} - R^{\mathsf{T}}\boldsymbol{\omega} = 0 \quad \text{in } \Omega_m, \tag{6a}$$

$$D\boldsymbol{\sigma} + \boldsymbol{f} = 0 \quad \text{in } \Omega_m, \tag{6b}$$

$$-R\boldsymbol{\sigma} = 0 \quad \text{in } \Omega_m, \tag{6c}$$

$$\boldsymbol{\lambda} = \boldsymbol{u} \quad \text{on } \Gamma_{ij}, \tag{6d}$$

$$\boldsymbol{u} = \widehat{\boldsymbol{u}} \quad \text{on } \Gamma_{\boldsymbol{u}}, \tag{6e}$$

$$\boldsymbol{t} = \widehat{\boldsymbol{t}} \quad \text{on } \Gamma_{\boldsymbol{t}}, \tag{6f}$$

$$\boldsymbol{t}_i + \boldsymbol{t}_j = 0 \quad \text{on } \Gamma_{ij}. \tag{6g}$$

Hybrid problem (6) is equivalent to the linear elasticity problem (2). The weak formulation derived from (5) is written as: For all subdomains Ω_m and all interfaces Γ_{ij}, given $\boldsymbol{f} \in \left[L^2(\Omega_m)\right]^3$ and $\widehat{\boldsymbol{u}} \in \left[H^{1/2}(\partial\Omega_m \cap \Gamma_{\boldsymbol{u}})\right]^3$, find $(\boldsymbol{\sigma}, \boldsymbol{u}, \boldsymbol{\omega}, \boldsymbol{\lambda}) \in [H_0(\mathrm{div}; \Omega_m; \partial\Omega_m \cap \Gamma_{\boldsymbol{t}})]^3 \times \left[L^2(\Omega_m)\right]^3 \times \left[L^2(\Omega_m)\right]^3 \times \left[H^{1/2}(\Gamma_{ij})\right]^3$ such that

$$\left(\overline{\boldsymbol{\sigma}}, C\boldsymbol{\sigma}\right)_{\Omega_m} + \left(\boldsymbol{u}, D\overline{\boldsymbol{\sigma}}\right)_{\Omega_m} - \left(\boldsymbol{\omega}, R\overline{\boldsymbol{\sigma}}\right)_{\Omega_m} - \sum_n \left\langle \boldsymbol{\lambda}, \overline{\boldsymbol{t}} \right\rangle_{\Gamma_{mn}} = \left\langle \widehat{\boldsymbol{u}}, \overline{\boldsymbol{t}} \right\rangle_{\partial\Omega_m \cap \Gamma_{\boldsymbol{u}}}, \quad \forall\, \overline{\boldsymbol{\sigma}} \in [H_0(\mathrm{div}; \Omega_m; \partial\Omega_m \cap \Gamma_{\boldsymbol{t}})]^3, \tag{7a}$$

$$\left(\overline{\boldsymbol{u}}, D\boldsymbol{\sigma}\right)_{\Omega_m} = -\left(\overline{\boldsymbol{u}}, \boldsymbol{f}\right)_{\Omega_m}, \quad \forall\, \overline{\boldsymbol{u}} \in \left[L^2(\Omega_m)\right]^3, \tag{7b}$$

$$-\left(\overline{\boldsymbol{\omega}}, R\boldsymbol{\sigma}\right)_{\Omega_m} = 0, \quad \forall\, \overline{\boldsymbol{\omega}} \in \left[L^2(\Omega_m)\right]^3, \tag{7c}$$

$$-\left\langle \overline{\boldsymbol{\lambda}}, \boldsymbol{t}_i + \boldsymbol{t}_j \right\rangle_{\Gamma_{ij}} = 0, \quad \forall\, \overline{\boldsymbol{\lambda}} \in \left[H^{1/2}(\Gamma_{ij})\right]^3. \tag{7d}$$

We call (7) the hybrid mixed weak formulation.

4. Numerical method

The exact sequence - the de Rham complex [16,17,34],

$$\mathbb{R} \hookrightarrow H^1(\Omega) \xrightarrow{\text{grad}} H(\mathrm{curl}; \Omega) \xrightarrow{\text{curl}} H(\mathrm{div}; \Omega) \xrightarrow{\text{div}} L^2(\Omega) \to 0, \tag{8}$$

is of essential importance for structure-preserving methods. For example, we have chosen $\boldsymbol{\sigma} \in [H(\mathrm{div}; \Omega)]^3$ and $\boldsymbol{f} \in \left[L^2(\Omega)\right]^3$ such that the equilibrium of forces, $D\boldsymbol{\sigma} + \boldsymbol{f} = \boldsymbol{0}$, can be exactly satisfied for the weak formulations. However, this does not guarantee that the equilibrium of forces is satisfied at the discrete level unless the finite dimensional function spaces used for the discretization also form a de Rham complex.

In this section, we will first introduce the construction of the *mimetic polynomial spaces* which, as will be seen, are able to form a discrete de Rham complex in either orthogonal or curvilinear meshes. These spaces have been used in the MSEM for various problems [2–6]. For the hMSEM, by extending the original mimetic polynomials to trace spaces and introducing the dual polynomials, a second de Rham complex in terms of particular discrete weak operators will be constructed. The two discrete de Rham complexes are then applied to the hybrid linear elasticity problem.

4.1. Mimetic polynomial spaces

The finite dimensional function spaces used in this paper are the mimetic polynomial spaces spanned by either the primal polynomials or their dual representations (dual polynomials). The primal polynomials are constructed using the Lagrange polynomials and the edge polynomials [36]. The dual polynomials are basically linear combinations of the primal polynomials.

4.1.1. Primal polynomials in $\mathbb{R}$

For completeness, we start with the well-known Lagrange polynomials. Given $(N+1)$ nodes, $-1 \le \xi_0 < \xi_1 < \cdots < \xi_N \le 1$, over interval $I = [-1, 1]$, the $(N+1)$ Lagrange polynomials of degree N are defined as

$$l_i(\xi) = \prod_{j=0, j\neq i}^{N} \frac{\xi - \xi_j}{\xi_i - \xi_j}, \quad i \in \{0, 1, 2, \cdots, N\},$$

which satisfy the so-called Kronecker delta property,

$$l_i\left(\xi_j\right) = \delta_{i,j} = \begin{cases} 1 & \text{if } i = j \\ 0 & \text{else} \end{cases}. \tag{9}$$

Examples of the Lagrange polynomials are shown in Fig. 1 (Left). Let $p^h(\xi)$ be a polynomial of degree N,

$$p^h(\xi) = \sum_{i=0}^{N} \mathrm{p}_i l_i(\xi). \tag{10}$$

If we take the derivative of $p^h(\xi)$, we get

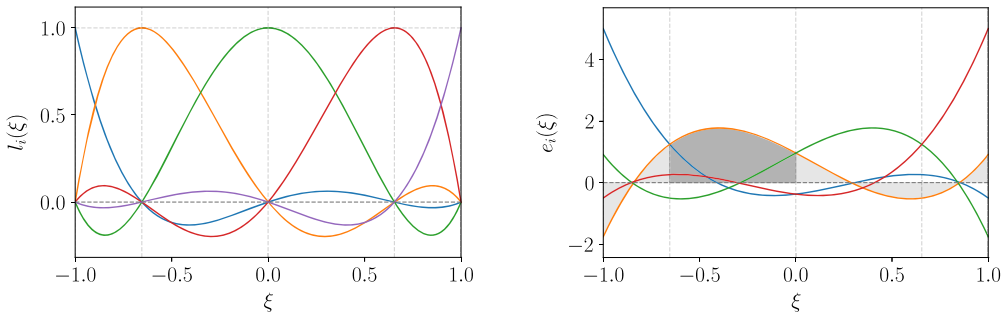

Fig. 1. Lagrange polynomials (Left) and edge polynomials (Right) derived from a set of 5 nodes, $-1 = \xi_0 < \xi_1 < \cdots < \xi_4 = 1$. The vertical gray dashed lines indicate the internal nodes ξ_1, ξ_2, ξ_3. The nodal Kronecker delta property (9) is obvious. The integral Kronecker delta property (12) can be seen, for example, from the edge polynomial $e_2(\xi)$ (orange solid line). Direct calculations will reveal that $\int_{\xi_1}^{\xi_2} e_2(\xi)\mathrm{d}\xi = 1$ and $\int_{\xi_{j-1}}^{\xi_j} e_2(\xi)\mathrm{d}\xi = 0,\ j \in \{1, 3, 4\}$. (For interpretation of the colors in the figure(s), the reader is referred to the web version of this article.)

$$\frac{\mathrm{d}p^h(\xi)}{\mathrm{d}\xi} = \sum_{i=0}^{N} \mathsf{p}_i \frac{\mathrm{d}l_i(\xi)}{\mathrm{d}\xi} = \sum_{i=1}^{N} \left[(\mathsf{p}_i - \mathsf{p}_{i-1}) \sum_{k=i}^{N} \frac{\mathrm{d}l_k(\xi)}{\mathrm{d}\xi} \right] = \sum_{i=1}^{N} \left[(\mathsf{p}_{i-1} - \mathsf{p}_i) \sum_{k=0}^{i-1} \frac{\mathrm{d}l_k(\xi)}{\mathrm{d}\xi} \right], \tag{11}$$

where the N polynomials of degree $(N-1)$ are the corresponding edge polynomials [36] denoted by $e_i(\xi)$,

$$e_i(\xi) = \sum_{k=i}^{N} \frac{\mathrm{d}l_k(\xi)}{\mathrm{d}\xi} = -\sum_{k=0}^{i-1} \frac{\mathrm{d}l_k(\xi)}{\mathrm{d}\xi}, \quad i \in \{1, 2, \cdots, N\}.$$

With Newton-Leibniz integral rule and the nodal Kronecker delta property (9), it is easy to see that the edge polynomials satisfy the Kronecker delta property in an integral sense, namely,

$$\int_{\xi_{j-1}}^{\xi_j} e_i(\xi)\mathrm{d}\xi = \delta_{i,j} = \begin{cases} 1 & \text{if } i = j \\ 0 & \text{else} \end{cases}. \tag{12}$$

Examples of edge polynomials are shown in Fig. 1 (Right). Now, we can write (11) as

$$q^h(\xi) = \frac{\mathrm{d}p^h(\xi)}{\mathrm{d}\xi} = \sum_{i=1}^{N} (\mathsf{p}_i - \mathsf{p}_{i-1})\, e_i(\xi) = \sum_{i=1}^{N} \mathsf{q}_i e_i(\xi). \tag{13}$$

If we collect the expansion coefficients or degrees of freedom of p^h and q^h, we obtain two vectors, $\underline{p}$ and $\underline{q}$,

$$\underline{p} = \begin{Bmatrix} \mathsf{p}_0 & \mathsf{p}_1 & \cdots & \mathsf{p}_N \end{Bmatrix}^{\mathsf{T}}, \quad \underline{q} = \begin{Bmatrix} \mathsf{q}_1 & \mathsf{q}_2 & \cdots & \mathsf{q}_N \end{Bmatrix}^{\mathsf{T}}. \tag{14}$$

Throughout the paper, underlined quantities will represent the vectors of expansion coefficients. From (13), we have

$$\underline{q} = \mathsf{E}_{\mathrm{d}} \underline{p},$$

where the linear operator E_{d},

$$\mathsf{E}_{\mathrm{d}} = \begin{Bmatrix} -1 & 1 & 0 & \cdots & 0 & 0 & 0 \\ 0 & -1 & 1 & \cdots & 0 & 0 & 0 \\ 0 & 0 & -1 & \cdots & 0 & 0 & 0 \\ \vdots & \vdots & \vdots & \ddots & \vdots & \vdots & \vdots \\ 0 & 0 & 0 & \cdots & -1 & 1 & 0 \\ 0 & 0 & 0 & \cdots & 0 & -1 & 1 \end{Bmatrix},$$

is called the *incidence matrix* which is a discrete counterpart of the derivative operator. The incidence matrix is a sparse matrix (if $N > 1$) and becomes sparser when N grows. It is also a topological matrix. For example, assuming N does not change and the degrees of freedom are labeled in a consistent way (the topology of the nodes does not change), if we use a different set of nodes or map the domain I into a different domain using a continuous mapping, the basis functions change, but the incidence matrix remains the same. One point to emphasize is that (13) is exact, which means that the discretization of the derivative operator with the incidence matrix E_{d} is exact [37,38].

The Lagrange polynomials and edge polynomials are the primal polynomials in $\mathbb{R}$. Let the finite dimensional polynomial spaces spanned by the Lagrange polynomials and the edge polynomials be denoted by L^N and $\mathrm{E}^{(N-1)}$ respectively. From

(10) and (13), we know that the range of the derivative operator on L^N is in $\mathrm{E}^{(N-1)}$. Therefore, we can conclude that L^N and $\mathrm{E}^{(N-1)}$ form the following de Rham complex,

$$\begin{array}{ccccc} \underline{\mathrm{L}}^N & \longleftarrow & \mathrm{L}^N & \xhookleftarrow{\subset} & H^1(I) \\ \downarrow{\scriptstyle \mathsf{E}_{\mathrm{d}}} & & \downarrow{\scriptstyle \mathrm{d}} & & \downarrow{\scriptstyle \mathrm{d}} \\ \underline{\mathrm{E}}^{(N-1)} & \longleftarrow & \mathrm{E}^{(N-1)} & \xhookleftarrow{\subset} & L^2(I) \end{array}$$

Here the underlined spaces $\underline{\mathrm{L}}^N$ and $\underline{\mathrm{E}}^{(N-1)}$ denote the spaces of expansion coefficient vectors of the elements in L^N and $\mathrm{E}^{(N-1)}$ respectively. This convention, in addition to the convention in (14), is also used throughout the paper.

4.1.2. Primal polynomials in $\mathbb{R}^3$

The primal polynomials in $\mathbb{R}^3$ are constructed with the primal polynomials (the Lagrange polynomials and the edge polynomials) in $\mathbb{R}$ using the tensor product. We consider the reference element $(\xi,\eta,\varsigma)\in\Omega_{\mathrm{ref}}=[-1,1]^3$ and three sets of nodes, $-1\le\xi_0<\xi_1<\cdots<\xi_{N_\xi}\le 1$, $-1\le\eta_0<\eta_1<\cdots<\eta_{N_\eta}\le 1$, and $-1\le\varsigma_0<\varsigma_1<\cdots<\varsigma_{N_\varsigma}\le 1$. The tensor product of the primal polynomials in $\mathbb{R}$ gives primal polynomials in $\mathbb{R}^3$ that span the following primal polynomial spaces,

$$\begin{aligned} P &:= \mathrm{L}^{N_\xi}\otimes\mathrm{L}^{N_\eta}\otimes\mathrm{L}^{N_\varsigma}, \\ E &:= \mathrm{E}^{(N_\xi-1)}\otimes\mathrm{L}^{N_\eta}\otimes\mathrm{L}^{N_\varsigma} \quad\times\quad \mathrm{L}^{N_\xi}\otimes\mathrm{E}^{(N_\eta-1)}\otimes\mathrm{L}^{N_\varsigma} \quad\times\quad \mathrm{L}^{N_\xi}\otimes\mathrm{L}^{N_\eta}\otimes\mathrm{E}^{(N_\varsigma-1)}, \\ S &:= \mathrm{L}^{N_\xi}\otimes\mathrm{E}^{(N_\eta-1)}\otimes\mathrm{E}^{(N_\varsigma-1)} \quad\times\quad \mathrm{E}^{(N_\xi-1)}\otimes\mathrm{L}^{N_\eta}\otimes\mathrm{E}^{(N_\varsigma-1)} \quad\times\quad \mathrm{E}^{(N_\xi-1)}\otimes\mathrm{E}^{(N_\eta-1)}\otimes\mathrm{L}^{N_\varsigma}, \\ V &:= \mathrm{E}^{(N_\xi-1)}\otimes\mathrm{E}^{(N_\eta-1)}\otimes\mathrm{E}^{(N_\varsigma-1)}, \end{aligned}$$

where the notations of the spaces, P, E, S, and V, stand for *points (nodes)*, *edges*, *surfaces*, and *volumes*. We use this notation because the degrees of freedom of corresponding elements represent values of the elements evaluated at the points or integrated over the edges, surfaces, or volumes. An element in S is written as

$$\boldsymbol{\alpha}^h(\xi,\eta,\varsigma)=\begin{Bmatrix}\alpha^h_\xi(\xi,\eta,\varsigma)\\ \alpha^h_\eta(\xi,\eta,\varsigma)\\ \alpha^h_\varsigma(\xi,\eta,\varsigma)\end{Bmatrix}=\begin{Bmatrix}\sum_{i=0}^{N_\xi}\sum_{j=1}^{N_\eta}\sum_{k=1}^{N_\varsigma}\mathsf{a}^\xi_{i,j,k}l_i(\xi)e_j(\eta)e_k(\varsigma)\\ \sum_{i=1}^{N_\xi}\sum_{j=0}^{N_\eta}\sum_{k=1}^{N_\varsigma}\mathsf{a}^\eta_{i,j,k}e_i(\xi)l_j(\eta)e_k(\varsigma)\\ \sum_{i=1}^{N_\xi}\sum_{j=1}^{N_\eta}\sum_{k=0}^{N_\varsigma}\mathsf{a}^\varsigma_{i,j,k}e_i(\xi)e_j(\eta)l_k(\varsigma)\end{Bmatrix},$$

and an element in V is written as

$$\beta^h(\xi,\eta,\varsigma)=\sum_{i=1}^{N_\xi}\sum_{j=1}^{N_\eta}\sum_{k=1}^{N_\varsigma}\mathsf{b}_{i,j,k}e_i(\xi)e_j(\eta)e_k(\varsigma).$$

If $\beta^h=\mathrm{div}\boldsymbol{\alpha}^h$, from Section 4.1.1, we know that their expansion coefficients satisfy

$$\mathsf{b}_{i,j,k}=\mathsf{a}^\xi_{i,j,k}-\mathsf{a}^\xi_{i-1,j,k}+\mathsf{a}^\eta_{i,j,k}-\mathsf{a}^\eta_{i,j-1,k}+\mathsf{a}^\varsigma_{i,j,k}-\mathsf{a}^\varsigma_{i,j,k-1}, \tag{15}$$

which basically implies the Gauss's theorem, see Remark 1. If we label all expansion coefficients of $\boldsymbol{\alpha}^h$ and β^h and put them into vectors $\underline{\boldsymbol{\alpha}}$ and $\underline{\beta}$, we get

$$\underline{\beta}=\mathsf{E}_{\mathrm{div}}\underline{\boldsymbol{\alpha}}, \tag{16}$$

where $\mathsf{E}_{\mathrm{div}}:\underline{S}\to\underline{V}$ is the incidence matrix representing the discrete divergence operator. For example, let $N_\xi=N_\varsigma=1$, $N_\eta=2$, and we label the coefficients of $\underline{\boldsymbol{\alpha}}$ and $\underline{\beta}$ as shown in Fig. 2. We have

$$\mathsf{E}_{\mathrm{div}}=\begin{Bmatrix}-1 & 0 & 1 & 0 & -1 & 1 & 0 & -1 & 0 & 1 & 0\\ 0 & -1 & 0 & 1 & 0 & -1 & 1 & 0 & -1 & 0 & 1\end{Bmatrix}.$$

Similarly, we can obtain $\mathsf{E}_{\mathrm{grad}}:\underline{P}\to\underline{E}$ and $\mathsf{E}_{\mathrm{curl}}:\underline{E}\to\underline{S}$. The fact that $\mathrm{curl}\cdot\mathrm{grad}(\cdot)\equiv 0$ and $\mathrm{div}\cdot\mathrm{curl}(\cdot)\equiv 0$ implies $\mathsf{E}_{\mathrm{curl}}\mathsf{E}_{\mathrm{grad}}\equiv\mathbf{0}$ and $\mathsf{E}_{\mathrm{div}}\mathsf{E}_{\mathrm{curl}}\equiv\mathbf{0}$.

Remark 1. If $\boldsymbol{\alpha}^h$ is the discrete ξ-direction stress $\boldsymbol{\sigma}^h_\xi$, and β^h is the discrete ξ-direction body force f^h_ξ, the ξ-direction equilibrium of forces for the volume $[\xi_{i-1},\xi_i]\times[\eta_{j-1},\eta_j]\times[\varsigma_{k-1},\varsigma_k]$ then implies $\mathrm{div}\boldsymbol{\sigma}^h_\xi+f^h_\xi=0$ or, in matrix format, $\mathsf{E}_{\mathrm{div}}\underline{\boldsymbol{\sigma}}_\xi+\underline{f}_\xi=0$ or, more directly,

$$\mathsf{t}^{\xi\xi}_{i,j,k}-\mathsf{t}^{\xi\xi}_{i-1,j,k}+\mathsf{t}^{\eta\xi}_{i,j,k}-\mathsf{t}^{\eta\xi}_{i,j-1,k}+\mathsf{t}^{\varsigma\xi}_{i,j,k}-\mathsf{t}^{\varsigma\xi}_{i,j,k-1}+\mathsf{f}^{\xi}_{i,j,k}=0,$$

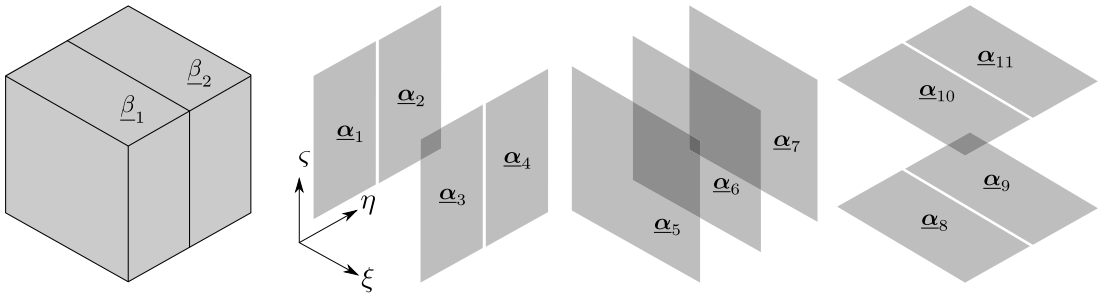

Fig. 2. An example of labeling the expansion coefficients of $\underline{\boldsymbol{\alpha}}$ and $\underline{\beta}$ for $N_\xi = N_\zeta = 1$ and $N_\eta = 2$.

where $\mathrm{t}_{i,j,k}$, the expansion coefficients of $\boldsymbol{\sigma}^h_\xi$, are the (integrated) surface tractions, $\mathrm{f}^\xi_{i,j,k}$, the expansion coefficients of f^h_ξ, are the integral values of the body force.

In summary, we have constructed the following de Rham complex,

$$\begin{array}{ccccc}
\underline{P} & \longleftarrow & P & \xhookrightarrow{\subset} & H^1(\Omega_{\text{ref}}) \\
\downarrow{\scriptstyle \mathsf{E}_{\text{grad}}} & & \downarrow{\scriptstyle \text{grad}} & & \downarrow{\scriptstyle \text{grad}} \\
\underline{E} & \longleftarrow & E & \xhookrightarrow{\subset} & H(\text{curl};\Omega_{\text{ref}}) \\
\downarrow{\scriptstyle \mathsf{E}_{\text{curl}}} & & \downarrow{\scriptstyle \text{curl}} & & \downarrow{\scriptstyle \text{curl}} \\
\underline{S} & \longleftarrow & S & \xhookrightarrow{\subset} & H(\text{div};\Omega_{\text{ref}}) \\
\downarrow{\scriptstyle \mathsf{E}_{\text{div}}} & & \downarrow{\scriptstyle \text{div}} & & \downarrow{\scriptstyle \text{div}} \\
\underline{V} & \longleftarrow & V & \xhookrightarrow{\subset} & L^2(\Omega_{\text{ref}})
\end{array}$$

For a comprehensive introduction to mimetic polynomial spaces, we refer to [2,3]. For spline basis function spaces of similar structures, we refer to [39,40].

4.1.3. Primal trace polynomials in $\mathbb{R}^3$

We consider the discrete vector valued function $\boldsymbol{\alpha}^h$ in S. The trace of $\boldsymbol{\alpha}^h$ on the face, for example, $(\xi,\eta,\zeta) \in \Gamma_{\xi^-} = -1 \times [-1,1] \times [-1,1]$ is

$$\mathrm{tr}_{\xi^-}\boldsymbol{\alpha}^h = \begin{Bmatrix} \alpha^h_\xi(-1,\eta,\zeta) \\ \alpha^h_\eta(-1,\eta,\zeta) \\ \alpha^h_\zeta(-1,\eta,\zeta) \end{Bmatrix} \cdot \begin{Bmatrix} -1 \\ 0 \\ 0 \end{Bmatrix} = -\sum_{i=0}^{N_\xi}\sum_{j=1}^{N_\eta}\sum_{k=1}^{N_\zeta} \mathrm{a}^\xi_{i,j,k} l_i(-1) e_j(\eta) e_k(\zeta) = \sum_{j=1}^{N_\eta}\sum_{k=1}^{N_\zeta} \mathrm{a}^{\xi^-}_{j,k} e_j(\eta) e_k(\zeta).$$

The primal trace polynomials $e_j(\eta)e_k(\zeta)$ then span a trace space on Γ_{ξ^-}. We denote this trace space by ∂S_{ξ^-}. If we have locally labeled the coefficients $\mathrm{a}^{\xi^-}_{j,k}$, we can collect and put them in a vector, $\underline{\alpha}_{\xi^-}$. It is clear that there is a linear operator N_{ξ^-} which maps $\underline{\boldsymbol{\alpha}}$ into $\underline{\alpha}_{\xi^-}$:

$$\underline{\alpha}_{\xi^-} = \mathsf{N}_{\xi^-}\underline{\boldsymbol{\alpha}}.$$

The matrix N_{ξ^-}, called the trace matrix [38], like the incidence matrices, is also a topological matrix. For example, for the configuration in Fig. 2,

$$\mathsf{N}_{\xi^-} = \begin{Bmatrix} -1 & 0 & 0 & 0 & 0 & 0 & 0 & 0 & 0 & 0 & 0 \\ 0 & -1 & 0 & 0 & 0 & 0 & 0 & 0 & 0 & 0 & 0 \end{Bmatrix}.$$

If we apply the above process to all 6 faces, we can obtain trace spaces,

$$\partial S_{\xi^-}, \quad \partial S_{\xi^+}, \quad \partial S_{\eta^-}, \quad \partial S_{\eta^+}, \quad \partial S_{\zeta^-}, \quad \partial S_{\zeta^+}, \tag{17}$$

and trace matrices,

$$\mathsf{N}_{\xi^-}, \quad \mathsf{N}_{\xi^+}, \quad \mathsf{N}_{\eta^-}, \quad \mathsf{N}_{\eta^+}, \quad \mathsf{N}_{\zeta^-}, \quad \mathsf{N}_{\zeta^+}. \tag{18}$$

Similarly, the trace spaces of P and E and corresponding trace matrices can be constructed.

4.1.4. Dual polynomials

We consider the primal polynomial space V, and let $\varphi^h, \phi^h \in V$. The L^2-inner product between φ^h and ϕ^h is

$$\left(\varphi^h, \phi^h\right)_{\Omega_{\text{ref}}} = \underline{\varphi}^{\mathsf{T}} \mathsf{M} \underline{\phi}, \tag{19}$$

where M is the mass matrix which is symmetric, and, because the primal polynomials are linearly independent, is also bijective and positive-definite. As a consequence, it is always invertible. The dual polynomials can then be defined as

$$\left\{\cdots, \widetilde{e}\widetilde{e}e_{i,j,k}(\xi,\eta,\varsigma), \cdots\right\}^{\mathsf{T}} := \mathsf{M}^{-1}\left\{\cdots, e_i(\xi)e_j(\eta)e_k(\varsigma), \cdots\right\}^{\mathsf{T}}.$$

These dual polynomials form another basis of the space V. See also equation (28) in [41]. From now on, we use the notation with a tilde to represent an element expanded with dual polynomials. For example, an element, ϕ^h,

$$\phi^h(\xi,\eta,\varsigma) = \sum_{i=1}^{N_\xi}\sum_{j=1}^{N_\eta}\sum_{k=1}^{N_\varsigma} \phi_{i,j,k} e_i(\xi)e_j(\eta)e_k(\varsigma),$$

in V has a unique dual representation, denoted by $\widetilde{\phi}^h$,

$$\widetilde{\phi}^h(\xi,\eta,\varsigma) = \sum_{i=1}^{N_\xi}\sum_{j=1}^{N_\eta}\sum_{k=1}^{N_\varsigma} \widetilde{\phi}_{i,j,k} \widetilde{e}\widetilde{e}e_{i,j,k}(\xi,\eta,\varsigma),$$

whose degrees of freedom are

$$\underline{\widetilde{\phi}} = \mathsf{M}\underline{\phi}. \tag{20}$$

Note that $\widetilde{\phi}^h$ is exactly equal to ϕ^h, but only their representations are different. Now, the L^2-inner product between φ^h and $\widetilde{\phi}^h$ is

$$\left(\varphi^h, \widetilde{\phi}^h\right)_{\Omega_{\text{ref}}} = \underline{\varphi}^{\mathsf{T}} \underline{\widetilde{\phi}}. \tag{21}$$

It looks trivial; if we insert (20) into (21), we immediately retrieve (19), but, in practice, it can significantly simplify the discretization as the L^2-inner product between them is equal to the vector inner product of their expansion coefficient vectors. More discussions will be given in Section 4.3. We can apply the same approach to other primal polynomials to construct dual polynomials or dual trace polynomials. For an example of the usage of the dual trace space, we refer to [24].

Examples.

1. If $\beta^h = \text{div}\boldsymbol{\alpha}^h \in V$ is expanded with primal polynomials and $\widetilde{\phi}^h \in V$ is expanded with dual polynomials, from (16) and (21), we have
$$\left(\widetilde{\phi}^h, \beta^h\right)_{\Omega_{\text{ref}}} = \left(\widetilde{\phi}^h, \text{div}\boldsymbol{\alpha}^h\right)_{\Omega_{\text{ref}}} = \underline{\widetilde{\phi}}^{\mathsf{T}} \mathsf{E}_{\text{div}} \underline{\boldsymbol{\alpha}}. \tag{22}$$
2. If $\boldsymbol{\alpha}^h \in S$ is expanded with primal polynomials and $\widehat{\phi} \in \partial S$ is expanded with dual trace polynomials, we have
$$\left\langle \widehat{\phi}, \text{tr}\boldsymbol{\alpha}^h \right\rangle_{\partial\Omega_{\text{ref}}} = \underline{\widehat{\phi}}^{\mathsf{T}} \mathsf{N} \underline{\boldsymbol{\alpha}}, \tag{23}$$
where the trace space $\partial S := \partial S_{\xi^-} \times \partial S_{\xi^+} \times \partial S_{\eta^-} \times \partial S_{\eta^+} \times \partial S_{\varsigma^-} \times \partial S_{\varsigma^+}$, see (17), and N can be obtained by assembling the trace matrices in (18). □

Remark 2. Given $\phi \in L^2(\Omega_{\text{ref}})$, to calculate the gradient of ϕ, since its space does not admit a strong gradient operation, we need to employ integration by parts and do it in a weaker way with respect to the inner product,

$$\int_\Omega \text{grad}\phi \cdot \boldsymbol{\alpha} \,\text{d}\Omega := \int_{\partial\Omega} \widehat{\phi}\boldsymbol{\alpha} \cdot \boldsymbol{n} \,\text{d}\Gamma - \int_\Omega \phi \,\text{div}\boldsymbol{\alpha} \,\text{d}\Omega.$$

At the discrete level, if we expand ϕ into $\widetilde{\phi}^h \in V$ with dual polynomials, expand $\widehat{\phi}$ into $\widehat{\phi}^h \in \partial S$ with dual trace polynomials, and expand $\boldsymbol{\alpha}$ into $\boldsymbol{\alpha}^h \in S$ with primal polynomials, we have

$$\left(\text{grad}\widetilde{\phi}^h, \boldsymbol{\alpha}^h\right)_{\Omega_{\text{ref}}} = \left\langle \widehat{\phi}^h, \text{tr}\boldsymbol{\alpha}^h \right\rangle_{\partial\Omega_{\text{ref}}} - \left(\widetilde{\phi}^h, \text{div}\boldsymbol{\alpha}^h\right)_{\Omega_{\text{ref}}}.$$

We then can define a *discrete weak gradient*, $\widetilde{\text{grad}} : V \times \partial S \to S$. Let $\widetilde{\vartheta}^h := \widetilde{\text{grad}}\left(\widetilde{\phi}^h, \widehat{\phi}\right) \in S$ be expanded with dual polynomials, from (22) and (23), we can find that

$$\underline{\widetilde{\vartheta}} = \mathsf{N}^{\mathsf{T}} \underline{\widehat{\phi}} - \mathsf{E}_{\text{div}}^{\mathsf{T}} \underline{\widetilde{\phi}}. \tag{24}$$

This discrete weak gradient essentially is an implementation of integration by parts using the introduced polynomials. Because the incidence matrix E_{div} and the trace matrix N are both topological, such an implementation leads to a simple approach for performing the weak gradient at the discrete level. Similarly, one can define $\widetilde{\text{curl}}$ and $\widetilde{\text{div}}$ and thus construct a second discrete de Rham complex [34]:

$$0 \leftarrow P \times 0 \xleftarrow{\widetilde{\text{div}}} E \times \partial P \xleftarrow{\widetilde{\text{curl}}} S \times \partial E \xleftarrow{\widetilde{\text{grad}}} V \times \partial S \hookleftarrow \mathbb{R}.$$

In the same way as shown for $\widetilde{\text{grad}}$, $\widetilde{\text{curl}}$ and $\widetilde{\text{div}}$ also have topological matrix representations consisting of the corresponding incidence matrix and trace matrix, which is beyond the scope of this paper. See [34] for a comprehensive explanation.

Note that the presented approach of constructing dual polynomials is the most straightforward one. For alternative approaches, we refer to, e.g., [32,33].

4.2. Coordinate transformation

The primal and dual polynomials introduced so far are just for the reference element Ω_{ref}. Let Ω_m be an arbitrary element and Φ_m be a $\mathcal{C}^1$ diffeomorphism, $\Phi_m \colon \Omega_{\text{ref}} \to \Omega_m$,

$$\begin{Bmatrix} x & y & z \end{Bmatrix}^{\mathsf{T}} = \Phi_m(\xi, \eta, \varsigma),$$

whose Jacobian matrix is denoted by $\mathcal{J}$. Let P_m, E_m, S_m, and V_m represent the corresponding mimetic polynomial spaces in Ω_m. The primal basis functions in Ω_m are obtained by transforming the primal polynomials in Ω_{ref} with the following transformations, [6,37]:

1. The transformation between $\psi^h(\xi, \eta, \varsigma) \in P$ and $\psi_m^h(x, y, z) \in P_m$ is given by
$$\psi_m^h(x, y, z) = \left(\psi^h \circ \Phi_m^{-1}\right)(x, y, z), \quad \psi^h(\xi, \eta, \varsigma) = \left(\psi_m^h \circ \Phi_m\right)(\xi, \eta, \varsigma).$$
2. The transformation between $\boldsymbol{\varphi}^h(\xi, \eta, \varsigma) \in E$ and $\boldsymbol{\varphi}_m^h(x, y, z) \in E_m$ is given by
$$\boldsymbol{\varphi}_m^h(x, y, z) = \left(\mathcal{J}^{\mathsf{T}}\right)^{-1}\left(\boldsymbol{\varphi}^h \circ \Phi_m^{-1}\right)(x, y, z), \quad \boldsymbol{\varphi}^h(\xi, \eta, \varsigma) = \mathcal{J}^{\mathsf{T}}\left(\boldsymbol{\varphi}_m^h \circ \Phi_m\right)(\xi, \eta, \varsigma).$$
3. The transformation between $\boldsymbol{\alpha}^h(\xi, \eta, \varsigma) \in S$ and $\boldsymbol{\alpha}_m^h(x, y, z) \in S_m$ is given by
$$\boldsymbol{\alpha}_m^h(x, y, z) = \frac{\mathcal{J}}{\det\mathcal{J}}\left(\boldsymbol{\alpha}^h \circ \Phi_m^{-1}\right)(x, y, z), \quad \boldsymbol{\alpha}^h(\xi, \eta, \varsigma) = \mathcal{J}^{-1}\det\mathcal{J}\left(\boldsymbol{\alpha}_m^h \circ \Phi_m\right)(\xi, \eta, \varsigma). \tag{25}$$
4. The transformation between $\beta^h(\xi, \eta, \varsigma) \in V$ and $\beta_m^h(x, y, z) \in V_m$ is given by
$$\beta_m^h(x, y, z) = \frac{1}{\det\mathcal{J}}\left(\beta^h \circ \Phi_m^{-1}\right)(x, y, z), \quad \beta^h(\xi, \eta, \varsigma) = \det\mathcal{J}\left(\beta_m^h \circ \Phi_m\right)(\xi, \eta, \varsigma).$$

For example, let $\boldsymbol{\sigma}^h \in [S]^3$ be the Cauchy stress tensor, the Piola transformation (25) converts between $\boldsymbol{\sigma}^h$ and the first Piola-Kirchhoff stress tensor $\boldsymbol{\sigma}_m^h \in [S_m]^3$.

Note that, although the mapping changes the primal polynomials and therefore changes the metric-dependent mass matrices, it does not affect the metric-independent topological incidence matrices. Thus we have the following de Rham complex for Ω_m,

$$\begin{array}{ccccc}
\underline{P}_m & \longleftarrow & P_m & \xhookrightarrow{\subset} & H^1(\Omega_m) \\
\downarrow{\scriptstyle \mathsf{E}_{\text{grad}}} & & \downarrow{\scriptstyle \text{grad}} & & \downarrow{\scriptstyle \text{grad}} \\
\underline{E}_m & \longleftarrow & E_m & \xhookrightarrow{\subset} & H(\text{curl};\, \Omega_m) \\
\downarrow{\scriptstyle \mathsf{E}_{\text{curl}}} & & \downarrow{\scriptstyle \text{curl}} & & \downarrow{\scriptstyle \text{curl}} \\
\underline{S}_m & \longleftarrow & S_m & \xhookrightarrow{\subset} & H(\text{div};\, \Omega_m) \\
\downarrow{\scriptstyle \mathsf{E}_{\text{div}}} & & \downarrow{\scriptstyle \text{div}} & & \downarrow{\scriptstyle \text{div}} \\
\underline{V}_m & \longleftarrow & V_m & \xhookrightarrow{\subset} & L^2(\Omega_m)
\end{array}$$

The way of constructing the dual polynomials remains the same, and, for example, the relations (22)-(24) are still valid in Ω_m. Therefore, we obtain the second discrete de Rham complex for Ω_m,

$$0 \leftarrow P_m \times 0 \xleftarrow{\widetilde{\text{div}}} E_m \times \partial P_m \xleftarrow{\widetilde{\text{curl}}} S_m \times \partial E_m \xleftarrow{\widetilde{\text{grad}}} V_m \times \partial S_m \hookleftarrow \mathbb{R}.$$

And, because the trace matrices are also topological, the matrix representations for the $\widetilde{\text{grad}}$, $\widetilde{\text{curl}}$ and $\widetilde{\text{div}}$ remain unchanged under the mapping.

4.3. Discretization

We now can present the discretization of the hybrid mixed weak formulation (7) with the mimetic polynomials constructed in previous subsection. Suppose Ω^h is an orthogonal or curvilinear conforming hexahedral mesh in the computational domain Ω and, for each element, e.g., Ω_m, there exists a $\mathcal{C}^1$ diffeomorphism Φ_m that maps the reference element Ω_{ref} into it. We first use the Gauss-Lobatto-Legendre (GLL) nodes as the basis nodes to construct particular GLL polynomial spaces, and, from now on, the aforementioned notations, for example S_m and V_m, refer to their transformations in Ω_m. We also set up the Gauss-Legendre (GL) polynomial spaces which are one degree lower, and we use the notation $\mathring{P}_m$ to denote corresponding nodal space. This particular choice is for the discrete rotation, $\boldsymbol{\omega}^h \in \left[\mathring{P}_m\right]^3$, which is the Lagrange multiplier that enforces the symmetry of the stress tensor or equilibrium of moments. For comparison and completeness, we will first briefly introduce the discretization with the mimetic spectral element method (MSEM) [6].

4.3.1. Mimetic spectral element method

With the MSEM, we discretize the mixed weak formulation (4) in a conventional continuous mesh. In each element Ω_m, the space $[S_m]^3$ is selected to approximate $[H(\nabla\cdot;\Omega_m)]^3$ for the stress $\boldsymbol{\sigma}$; the space $[V_m]^3$ is selected to approximate $\left[L^2(\Omega_m)\right]^3$ for the body force $\boldsymbol{f}$; the space $\left[\mathring{P}_m\right]^3$ is selected to approximate $\left[L^2(\Omega_m)\right]^3$ for the displacement $\boldsymbol{u}$ and the rotation $\boldsymbol{\omega}$. All discrete variables are expanded with the primal polynomials. Such a discretization will eventually lead to the following discrete system,

$$\begin{Bmatrix} \mathbf{M}_m & (\mathbf{WE})^{\mathsf{T}} & -\mathbf{R}_m^{\mathsf{T}} \\ \mathbf{WE} & \mathbf{0} & \mathbf{0} \\ -\mathbf{R}_m & \mathbf{0} & \mathbf{0} \end{Bmatrix} \begin{Bmatrix} \underline{\boldsymbol{\sigma}} \\ \underline{\boldsymbol{u}} \\ \underline{\boldsymbol{\omega}} \end{Bmatrix} = \begin{Bmatrix} \mathbf{B}_m \widehat{\underline{\boldsymbol{u}}} \\ -\mathbf{W}\underline{\boldsymbol{f}} \\ \mathbf{0} \end{Bmatrix}. \tag{26}$$

Comparing this discrete system to the mixed weak formulation (4) reveals what each entry represents. Note that $\mathbf{E}$ represents the metric-independent topological incidence matrix, the matrix $\mathbf{W}$ is a dense matrix for the inner product between elements from $\left[\mathring{P}_m\right]^3$ and $[V_m]^3$, and the matrix $\mathbf{B}_m$ is a boundary integral matrix. For more insights of (26), see equations (20) and (21) in [6]. We denote the left hand side local matrix for element Ω_m by $\mathbb{F}_m$. Once the discrete systems for all elements are constructed locally, we can assemble them, which ensures the continuity of the surface traction across elements and leads to a global system. This leads to a global linear system ready to be solved, and we denote its left hand side global matrix by $\mathbb{F}$.

4.3.2. Hybrid mimetic spectral element method

With the hybrid mimetic spectral element method (hMSEM), we discretize the hybrid mixed weak formulation (7) in a discontinuous mesh where we consider each element as a separate subdomain. In element Ω_m, the same finite dimensional spaces as mentioned in Section 4.3.1 are selected to approximate the spaces for $\boldsymbol{\sigma}$, $\boldsymbol{\omega}$, and $\boldsymbol{f}$. While, for $\boldsymbol{u}$, the space $[V_m]^3$ is selected, and, to obtain a higher sparsity, it is expanded using the dual polynomials. To approximate the spaces $\left[H^{1/2}(\cdot)\right]^3$ for the Lagrange multiplier $\boldsymbol{\lambda}$, the spaces $\left[\partial S_{(\cdot)}\right]^3$ with a dual polynomial basis are selected. With these selections, we can obtain the following discrete hybrid system:

$$\begin{Bmatrix} \mathbf{M}_m & \mathbf{E}^{\mathsf{T}} & -\mathbf{R}_m^{\mathsf{T}} & -\mathbf{N}_\circ^{\mathsf{T}} \\ \mathbf{E} & \mathbf{0} & \mathbf{0} & \mathbf{0} \\ -\mathbf{R}_m & \mathbf{0} & \mathbf{0} & \mathbf{0} \\ -\mathbf{N}_\circ & \mathbf{0} & \mathbf{0} & \mathbf{0} \end{Bmatrix} \begin{Bmatrix} \underline{\boldsymbol{\sigma}} \\ \underline{\boldsymbol{u}} \\ \underline{\boldsymbol{\omega}} \\ \underline{\boldsymbol{\lambda}} \end{Bmatrix} = \begin{Bmatrix} \mathbf{N}_{\widehat{\boldsymbol{u}}}^{\mathsf{T}} \widehat{\underline{\boldsymbol{u}}} \\ -\underline{\boldsymbol{f}} \\ \mathbf{0} \\ \mathbf{0} \end{Bmatrix}. \tag{27}$$

For $\boldsymbol{\sigma}$ and $\boldsymbol{\omega}$, the expansions are the same for MSEM and hMSEM. We have

$$\left(\overline{\boldsymbol{\sigma}}^h, C\boldsymbol{\sigma}^h\right)_{\Omega_m} = \underline{\overline{\boldsymbol{\sigma}}}^{\mathsf{T}} \mathbf{M}_m \underline{\boldsymbol{\sigma}}, \quad \overline{\boldsymbol{\sigma}}^h,\ \boldsymbol{\sigma}^h \in [S_m]^3,$$

and

$$\left(\overline{\boldsymbol{\omega}}^h, R\boldsymbol{\sigma}^h\right)_{\Omega_m} = \underline{\overline{\boldsymbol{\omega}}}^{\mathsf{T}} \mathbf{R}_m \underline{\boldsymbol{\sigma}}, \quad \overline{\boldsymbol{\omega}}^h \in \left[\mathring{P}_m\right]^3,\ \boldsymbol{\sigma}^h \in [S_m]^3.$$

From (22), we know that

$$\left(\overline{\boldsymbol{u}}^h, D\boldsymbol{\sigma}^h\right)_{\Omega_m} = \underline{\overline{\boldsymbol{u}}}^{\mathsf{T}}\mathbf{E}\underline{\boldsymbol{\sigma}}, \quad \overline{\boldsymbol{u}}^h \in [V_m]^3\,,\ \boldsymbol{\sigma}^h \in [S_m]^3\,.$$

Using the symmetry, the discrete terms with $\mathbf{R}_m^{\mathsf{T}}$ and $\mathbf{E}^{\mathsf{T}}$ can be derived. The trace matrices, $\mathbf{N}_\circ$ and $\mathbf{N}_{\widehat{\boldsymbol{u}}}$, follow from

$$\left\langle \boldsymbol{\lambda}^h, \overline{\boldsymbol{t}}^h \right\rangle_{\partial\Omega_m \setminus \partial\Omega_m \cap \Gamma_{\boldsymbol{u}}} \overset{(23)}{=} \underline{\overline{\boldsymbol{\sigma}}}^{\mathsf{T}} \mathbf{N}_\circ^{\mathsf{T}} \underline{\boldsymbol{\lambda}}, \quad \boldsymbol{\lambda}^h \in [\partial S_\circ]^3\,,\ \overline{\boldsymbol{t}}^h \in \left[(\partial S_\circ)'\right]^3\,, \tag{28}$$

and

$$\left\langle \widehat{\boldsymbol{u}}^h, \overline{\boldsymbol{t}}^h \right\rangle_{\partial\Omega_m \cap \Gamma_{\boldsymbol{u}}} \overset{(23)}{=} \underline{\overline{\boldsymbol{\sigma}}}^{\mathsf{T}} \mathbf{N}_{\widehat{\boldsymbol{u}}}^{\mathsf{T}} \underline{\widehat{\boldsymbol{u}}}, \quad \widehat{\boldsymbol{u}}^h \in [\partial S_{\widehat{\boldsymbol{u}}}]^3\,,\ \overline{\boldsymbol{t}}^h \in \left[(\partial S_{\widehat{\boldsymbol{u}}})'\right]^3\,. \tag{29}$$

For example, if $\partial\Omega_m \cap \Gamma_{\boldsymbol{u}} = \Gamma_{\xi^-}$, we have

$$\partial S_\circ = \partial S_{\xi^+} \times \partial S_{\eta^-} \times \partial S_{\eta^+} \times \partial S_{\zeta^-} \times \partial S_{\zeta^+}, \quad \partial S_{\widehat{\boldsymbol{u}}} = \partial S_{\xi^-},$$

and trace matrices $\mathbf{N}_\circ$ and $\mathbf{N}_{\widehat{\boldsymbol{u}}}$ then can be obtained by assembling the corresponding trace matrices in (18). In particular, if Ω_m is an internal element, we have $\mathbf{N}_{\widehat{\boldsymbol{u}}} = \mathbf{0}$, and, if the mesh only has one element Ω_0 and $\Gamma_{\boldsymbol{u}} = \partial\Omega = \partial\Omega_0$, we have $\mathbf{N}_\circ = \mathbf{0}$, and the discrete hybrid system becomes

$$\begin{Bmatrix} \mathbf{M}_0 & \mathbf{E}^{\mathsf{T}} & -\mathbf{R}_0^{\mathsf{T}} \\ \mathbf{E} & \mathbf{0} & \mathbf{0} \\ -\mathbf{R}_0 & \mathbf{0} & \mathbf{0} \end{Bmatrix} \begin{Bmatrix} \underline{\boldsymbol{\sigma}} \\ \underline{\boldsymbol{u}} \\ \underline{\boldsymbol{\omega}} \end{Bmatrix} = \begin{Bmatrix} \mathbf{N}^{\mathsf{T}} \underline{\widehat{\boldsymbol{u}}} \\ -\underline{\boldsymbol{f}} \\ \mathbf{0} \end{Bmatrix}. \tag{30}$$

A comparison between this system and (26) clearly reveals that, by using the dual spaces, extra sparsity and simplification are gained due to the absence of $\mathbf{W}$ and the replacement of $\mathbf{B}_m$ by $\mathbf{N}^{\mathsf{T}}$ ($\mathbf{W}$ is a dense matrix and $\mathbf{B}_m$ is a dense and metric-dependent matrix).

Remark 3. To gain the extra sparsity and simplification, we only need to use, in (28) and (29), the fact that the L^2-inner product between an element expanded with primal polynomials and an element expanded with dual polynomials is just the vector inner product between their expansion coefficient vectors. Therefore, we do not need to explicitly construct the dual polynomials for the discretization. After solving the system, if we want to reconstruct those solutions expanded with the dual polynomials, the dual polynomials have to be constructed, which is relatively inexpensive because they can be constructed locally and, therefore, in parallel. Alternatively, we can convert the dual degrees of freedom to primal ones, see (20), and reconstruct them with the primal basis polynomials. This can also be done element-by-element.

Following the fact that the mass matrix $\mathbf{M}_m$ is positive definite, a sufficient condition of the discrete system (27) being well-posed is that matrices $\mathbf{E}$, $\mathbf{R}_m$ and $\mathbf{N}_\circ$ are surjective [42]. By construction, matrices $\mathbf{E}$ and $\mathbf{N}_\circ$ are surjective (see Section 4). By approximating the space for the rotation $\boldsymbol{\omega}^h$ using nodal spaces based on Gauss nodes, matrix $\mathbf{R}_m$ is surjective. A detailed analysis about choosing the approximation for the rotation $\boldsymbol{\omega}^h$ can be found in Section 10 of [6].

As elements are now discontinuous, only the trace variable $\boldsymbol{\lambda}$ needs to be solved in a global sense. For neatness, we now write the discrete hybrid system (27) as

$$\begin{Bmatrix} A & B^{\mathsf{T}} & C^{\mathsf{T}} & D^{\mathsf{T}} \\ B & \mathbf{0} & \mathbf{0} & \mathbf{0} \\ C & \mathbf{0} & \mathbf{0} & \mathbf{0} \\ D & \mathbf{0} & \mathbf{0} & \mathbf{0} \end{Bmatrix} \begin{Bmatrix} \underline{\boldsymbol{\sigma}} \\ \underline{\boldsymbol{u}} \\ \underline{\boldsymbol{\omega}} \\ \underline{\boldsymbol{\lambda}} \end{Bmatrix} = \begin{Bmatrix} \boldsymbol{a} \\ \boldsymbol{b} \\ \mathbf{0} \\ \mathbf{0} \end{Bmatrix}.$$

By applying the Schur complement, we can derive a local system for $\underline{\boldsymbol{\lambda}}$:

$$\mathbb{S}_m \underline{\boldsymbol{\lambda}} = \boldsymbol{\rho}, \tag{31}$$

where

$$\begin{aligned}
\mathbb{S}_m &= DA^{-1}D^{\mathsf{T}} - D\mathbb{B}D^{\mathsf{T}} - \mathbb{D}\mathbb{C}^{-1}\mathbb{D}^{\mathsf{T}},\\
\boldsymbol{\rho} &= \boldsymbol{\rho}_a + \boldsymbol{\rho}_b,\\
\boldsymbol{\rho}_a &= \left[\left(DA^{-1} - D\mathbb{B}\right) - \mathbb{D}\mathbb{C}^{-1}\left(CA^{-1} - C\mathbb{B}\right)\right]\boldsymbol{a},\\
\boldsymbol{\rho}_b &= \left(DA^{-1}B^{\mathsf{T}}\mathbb{A}^{-1} - \mathbb{D}\mathbb{C}^{-1}CA^{-1}B^{\mathsf{T}}\mathbb{A}^{-1}\right)\boldsymbol{b},\\
\mathbb{D} &= DA^{-1}C^{\mathsf{T}} - D\mathbb{B}C^{\mathsf{T}},\\
\mathbb{C} &= CA^{-1}C^{\mathsf{T}} - C\mathbb{B}C^{\mathsf{T}},\\
\mathbb{B} &= A^{-1}B^{\mathsf{T}}\mathbb{A}^{-1}BA^{-1},
\end{aligned}$$

$$\mathbb{A} = BA^{-1}B^{\mathsf{T}}.$$

The linear operator $\mathbb{S}_m$ is usually called the discrete Steklov-Poincaré operator or the Schur matrix [38,43]. Assembling local systems (31) for all elements gives a global system for $\underline{\boldsymbol{\lambda}}$ whose the left hand side matrix is denoted by $\mathbb{S}$. Once this system is solved, solving remaining local systems for $\underline{\boldsymbol{\sigma}}$, $\underline{\boldsymbol{u}}$, and $\underline{\boldsymbol{\omega}}$ becomes trivial.

Remark 4. Note that we have considered each element as a discontinuous subdomain. Alternatively, we can place multiple elements in one subdomain and use the Lagrange multiplier to couple the big subdomains. For example, see [44]. This gives more freedom for the hybridization.

Remark 5. With the hybridization, the total number of degrees of freedom increases, but the number of the interface degrees of freedom is relatively small. As a result, $\mathbb{S}$ (the global system of hMSEM) is much smaller than $\mathbb{F}$ (the global system of MSEM). We will use $\sharp_{(\cdot)}$ to represent the size of a square matrix. For example, $\mathbb{S}$ is a $\sharp_{\mathbb{S}}$ by $\sharp_{\mathbb{S}}$ matrix. If, for example, the degree of the GLL polynomials is N ($N_\xi = N_\eta = N_\varsigma = N \geq 1$), we will have

$$\sharp_{\mathbb{S}} = 3(I + B_{\boldsymbol{t}})N^2,$$

and

$$\sharp_{\mathbb{F}} = 3M\left[3N^2(N+1) + 2N^3\right] - 3(I + B_{\boldsymbol{t}})N^2,$$

where I is the total number of internal element interfaces, $B_{\boldsymbol{t}}$ is the number of element faces on the boundary $\Gamma_{\boldsymbol{t}}$, and M is the total number of elements. And we have

$$6M = 2I + B = 2I + B_{\boldsymbol{t}} + B_{\boldsymbol{u}}$$

if $B_{\boldsymbol{u}}$ is the number of element faces on the boundary $\Gamma_{\boldsymbol{u}}$ and B is the total number of element faces on the boundary. Let $\chi = I/B \in [0, \infty)$ and $\varrho = B_{\boldsymbol{t}}/B \in [0, 1)$, we can get the following system size ratio,

$$\frac{\sharp_{\mathbb{S}}}{\sharp_{\mathbb{F}}} = \frac{6\chi + 6\varrho}{10\chi N - 6\varrho + 5N + 3},$$

which decreases when χ or N increases or ϱ decreases. This ratio reveals how efficient the hMSEM is in terms of decreasing the size of the system to be solved. See (32) and Table 2 for some examples.

The hMSEM, compared to the MSEM, benefits from the extra simplicity during the discretization and leads to linear systems that are easier to solve. As for the accuracy, although the hMSEM will not improve the accuracy for $\boldsymbol{u}^h$ and $\boldsymbol{\omega}^h$ in terms of the L^2-error and for $\boldsymbol{\sigma}^h$ in terms of the $H(\mathrm{div})$-error, it improves the accuracy for $\boldsymbol{u}^h$ in terms of the $\widetilde{H}^1$-error (with respect to the discrete weak gradient operator $\widetilde{\mathrm{grad}}$). When we compute the discrete weak gradient of $\boldsymbol{u}^h$, the solution of the Lagrange multiplier, $\boldsymbol{\lambda}^h$, can serve as the boundary value, see Remark 2. Let $\boldsymbol{q}^h$ be the discrete weak gradient of $\boldsymbol{u}^h$,

$$\boldsymbol{q}^h := \widetilde{\mathrm{grad}}\left(\boldsymbol{u}^h, \boldsymbol{\lambda}^h\right).$$

Then we get

$$\underline{\boldsymbol{q}}^h = \mathbf{N}^{\mathsf{T}}\underline{\boldsymbol{\lambda}}^h - \mathbf{E}^{\mathsf{T}}\underline{\boldsymbol{u}}^h.$$

As a result, we can obtain superconvergence: The convergence rate of the $\widetilde{H}^1$-error of $\boldsymbol{u}^h$ is the same as (instead of one order lower than) that of the L^2-error under h-refinements (for example, see Fig. 7).

5. Numerical results

To demonstrate the proposed method, we apply it to three tests: A patch test, a manufactured solution test and a test with a singularity. In order not to pollute the results by the linear solver, we use a direct solver for all tests.

5.1. Patch test

We do a patch test in the domain $(x, y, z) \in \Omega = [-1, 1]^3$ for polynomial degree $N_\xi = N_\eta = N_\varsigma = N$ with the analytical solution for the displacement field given by

$$u_x = x^2yz^2 + 3xy^2z - 2z, \quad u_y = (x + 2y - z)^2, \quad u_z = (3x - y)^2 + xyz^2.$$

Analytical solutions for the rotation, stress, and body force follow. An orthogonal mesh of $2 \times 2 \times 2$ uniformly distributed elements (unit cubes) is set up, boundaries are set to $\Gamma_{\boldsymbol{u}} = \partial\Omega$, $\Gamma_{\boldsymbol{t}} = \emptyset$, and material properties are set to $E = 1$, $\nu = 0.3$. We

Table 1
Results of the patch test.

N	$\left\|\boldsymbol{u}^h\right\|_{H^1\text{-error}}$	$\left\|\boldsymbol{\omega}^h\right\|_{L^2\text{-error}}$	$\left\|\boldsymbol{\sigma}^h\right\|_{H(\text{div})\text{-error}}$	$\left\|R\boldsymbol{\sigma}^h\right\|_{L^2\text{-error}}$	$\left\|D\boldsymbol{\sigma}^h+\boldsymbol{f}^h\right\|_{L^\infty\text{-error}}$
1	1.65418E+01	8.39351E+00	1.30794E+01	6.73218E+00	6.21725E−15
2	2.21819E+00	2.37423E−01	9.64492E−01	8.77608E−02	2.37286E−13
3	7.20554E−13	7.70876E−13	1.19742E−12	7.88552E−13	5.67179E−12

solve the linear elasticity problem with the hMSEM and expect that the solutions converge down to the machine precision when $N \geq 3$. Results shown in Table 1 verify our expectation. The constant equilibrium of forces, demonstrated by the results of the L^∞-error of $\left(D\boldsymbol{\sigma}^h+\boldsymbol{f}^h\right)$, shows that the discretization of the divergence operator with the incidence matrix is exact.

5.2. Manufactured solution

In this test, we investigate the performance (both accuracy and efficiency) of the proposed hMSEM and compare it with that of the MSEM in both orthogonal and curvilinear meshes using a manufactured solution. The manufactured solution is taken from [11]. Its analytical solution for the displacement field is given as

$$u_x=-\frac{3F\nu}{4E}xyz,\quad u_y=\frac{F}{8E}\left[3\nu z\left(x^2-y^2\right)-z^3\right],\quad u_z=\frac{F}{8E}\left[3yz^2+\nu y\left(y^2-3x^2\right)\right]+\frac{2\left(1+\nu\right)}{E}U(x,y),$$

where F is a load coefficient, and

$$U(x,y)=\frac{F\left(3y-y^3\right)}{8}+\frac{F\nu\left(3x^2-1\right)y}{8\left(1+\nu\right)}-\frac{3F\nu}{2\pi^2\left(1+\nu\right)}\sum_{n=1}^{\infty}\frac{(-1)^n}{n^3\pi\cosh(n\pi)}\cos(n\pi x)\sinh(n\pi y).$$

The analytical solutions for the rotation, stress, and body force are

$$\omega_x=\frac{3F}{8E}\left(1+\frac{2}{3}\nu-y^2+z^2\right)-\frac{3F\nu}{2\pi^2E}\sum_{n=1}^{\infty}\frac{(-1)^n}{n^2\cosh(n\pi)}\cos(n\pi x)\cosh(n\pi y),$$

$$\omega_y=-\frac{3F\nu}{4E}\left[xy-\frac{2}{\pi^2}\sum_{n=1}^{\infty}\frac{(-1)^n}{n^2\cosh(n\pi)}\sin(n\pi x)\sinh(n\pi y)\right],\quad \omega_z=\frac{3F\nu xz}{4E},$$

$$\sigma_{xx}=\sigma_{yy}=\sigma_{xy}=\sigma_{yx}=0,\quad \sigma_{zz}=\frac{3F}{4}yz,\quad \sigma_{xz}=\sigma_{zx}=\frac{3F\nu}{2\pi^2\left(1+\nu\right)}\sum_{n=1}^{\infty}\frac{(-1)^n}{n^2\cosh(n\pi)}\sin(n\pi x)\sinh(n\pi y),$$

$$\sigma_{yz}=\sigma_{zy}=\frac{3F\left(1-y^2\right)}{8}+\frac{F\nu\left(3x^2-1\right)}{8\left(1+\nu\right)}-\frac{3F\nu}{2\pi^2\left(1+\nu\right)}\sum_{n=1}^{\infty}\frac{(-1)^n}{n^2\cosh(n\pi)}\cos(n\pi x)\cosh(n\pi y),$$

$$f_x=f_y=f_z=0.$$

Material properties E, ν, and the load coefficient F are set to $E=20$, $\nu=0.3$, and $F=10$.

The computational domain is selected to be $(x,y,z)\in\Omega=[0,1]^3$, and the boundary $\Gamma_{\boldsymbol{t}}$ is selected to be the face $x=1$. To generate the mesh, we first generate an orthogonal mesh of $M=K^3$ uniformly distributed elements, $(r,s,t)\in\mathring{\Omega}_{i,j,k}=\left[\frac{i-1}{K},\frac{i}{K}\right]\times\left[\frac{j-1}{K},\frac{j}{K}\right]\times\left[\frac{k-1}{K},\frac{k}{K}\right]$ $(i,j,k=1,2,\cdots,K)$, in the Cartesian domain $(r,s,t)\in\mathring{\Omega}=[0,1]^3$. The mesh in Ω is then obtained using a mapping $\mathring{\Phi}:\mathring{\Omega}\to\Omega$,

$$\begin{Bmatrix}x\\y\\z\end{Bmatrix}=\mathring{\Phi}(r,s,t)=\begin{Bmatrix}\Phi^x(r,s,t)\\\Phi^y(r,s,t)\\\Phi^z(r,s,t)\end{Bmatrix}=\begin{Bmatrix}r+c\sin(\pi r)\sin(\pi s)\sin(\pi t)\\s+c\sin(\pi r)\sin(\pi s)\sin(\pi t)\\t+c\sin(\pi r)\sin(\pi s)\sin(\pi t)\end{Bmatrix},$$

where c is a deformation coefficient. When $c=0$, the mesh is orthogonal. When $c\neq0$, the mesh is curvilinear. The transformation mapping, $\Phi_{i,j,k}:\Omega_{\text{ref}}\to\Omega_{i,j,k}$, then is given by

$$\Phi_{i,j,k}=\mathring{\Phi}\circ\Xi_{i,j,k},$$

where $\Xi_{i,j,k}$ is the linear transformation that maps Ω_{ref} into $\mathring{\Omega}_{i,j,k}$. Two examples of the mesh are shown in Fig. 3.

With this configuration, the mesh has $I=3K^2\left(K-1\right)$ internal element interfaces, $B=6K^2$ element faces on the boundary among which $B_{\boldsymbol{t}}=K^2$ are on $\Gamma_{\boldsymbol{t}}$. Therefore, we have $\chi=I/B=\left(K-1\right)/2$, $\varrho=B_{\boldsymbol{t}}/B=1/6$. The polynomial degree is set to be $N_\xi=N_\eta=N_\varsigma=N$. As a result, we can obtain the following system size ratio,

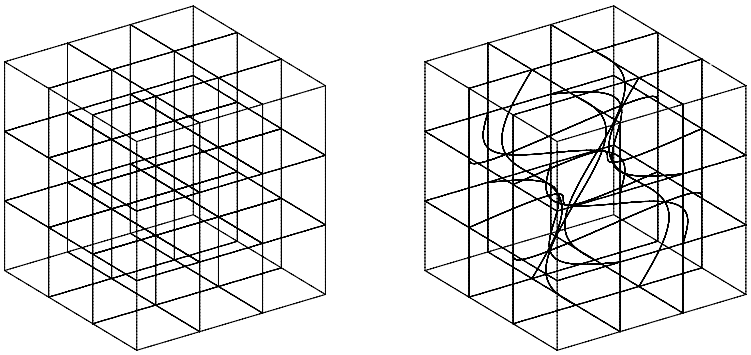

Fig. 3. Meshes of 3^3 elements for $c = 0$ (Left) and $c = 0.25$ (Right).

Table 2
Some samples of the system size ratio (32).

N	K					
	2	4	6	8	10	12
1	0.333333	0.454545	0.5	0.523810	0.538462	0.548387
3	0.125	0.161290	0.173913	0.180328	0.184211	0.186813
5	0.076923	0.098039	0.105263	0.108911	0.111111	0.112583

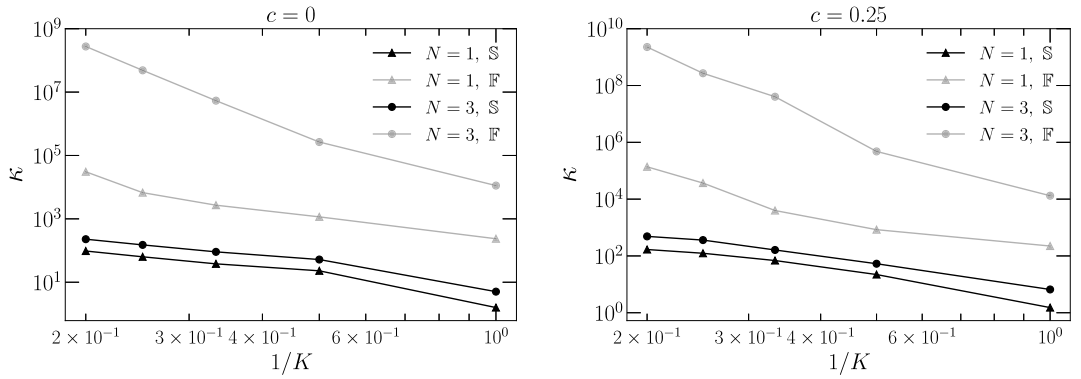

Fig. 4. Condition number comparison of $\mathbb{S}$ and $\mathbb{F}$ for $N \in \{1, 3\}$, $K \in \{1, 2, 3, 4, 5\}$, and $c \in \{0, 0.25\}$.

$$\frac{\sharp_{\mathbb{S}}}{\sharp_{\mathbb{F}}} = \frac{3K-2}{5KN+2}, \tag{32}$$

see Remark 5. It is clear from this ratio that the hybridized method has a increasingly better performance compared to the non-hybridized method as the polynomial degree N increases. And for a given N, the ratio increases and approaches the limit $\frac{3}{5N}$ as K increases. To give readers a more explicit impression, we provide some samples of this ratio in Table 2. In Fig. 4, we compare the condition numbers of the global systems. It is seen that the condition number of $\mathbb{S}$ is much smaller than that of $\mathbb{F}$ for certain N and K, which is not surprising because $\mathbb{S}$ is much smaller. A more interesting observation is that the former increases in a significantly lower speed under refinements. These results imply that the hMSEM, compared to the MSEM, needs far less computational power in the same mesh. In Fig. 5 where eigenspectra of $\mathbb{S}$ are present, we can see that all eigenvalues are away from zero. This supports the statement that the proposed hMSEM is free of spurious kinematic modes; $\mathbb{S}$ is not singular.

We then compare the accuracy of the hMSEM to that of the MSEM. Results are shown in Table 3. It can be seen that the hMSEM and the MSEM have the same accuracy with respect to the L^2-error of the solutions $\boldsymbol{u}^h$, $\boldsymbol{\omega}^h$, and $\boldsymbol{\sigma}^h$ for different basis function degrees ($N = 1, 3$) and element densities ($K = 2, 4, 6$) regardless of whether we are considering orthogonal meshes ($c = 0$) or heavily distorted meshes ($c = 0.25$). Note that, in this case,

$$\left\| \boldsymbol{\sigma}^h \right\|_{L^2\text{-error}} = \left\| \boldsymbol{\sigma}^h \right\|_{H(\text{div})\text{-error}},$$

because $D\boldsymbol{\sigma}^h = -\boldsymbol{f} = \boldsymbol{0}$ is exactly satisfied, see Fig, 8.

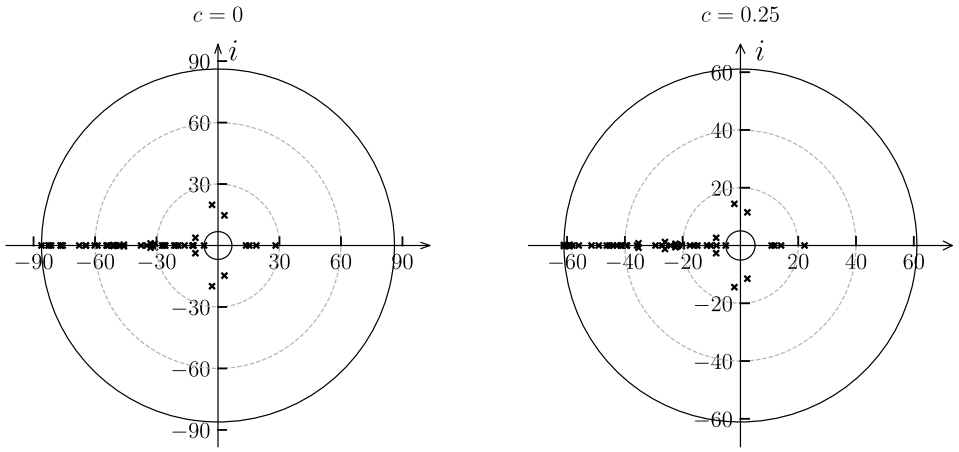

Fig. 5. Eigenspectra of $\mathbb{S}$ for $N = 1$, $K = 2$, and $c \in \{0, 0.25\}$. The radii of the black circles are the moduli of the eigenvalues of the maximum or minimum modulus.

Table 3
Results of $\|\boldsymbol{x}\|_{L^2\text{-error}}$ and $\|\boldsymbol{x} - \boldsymbol{x}'\|_{L^2\text{-norm}}$ (in brackets), where $\boldsymbol{x}$ and $\boldsymbol{x}'$ are solutions of the hMSEM and MSEM respectively, for $N \in \{1, 3\}$, $K \in \{2, 4, 6\}$, and $c \in \{0, 0.25\}$.

$\boldsymbol{x}$	K	$N = 1$		$N = 3$	
		$c = 0$	$c = 0.25$	$c = 0$	$c = 0.25$
$\boldsymbol{u}^h$	2	6.4029E−2(2.05E−16)	1.9534E−1(2.79E−16)	3.8024E−4(5.57E−16)	2.9940E−2(1.70E−15)
	4	3.2265E−2(5.40E−16)	1.1353E−1(4.61E−16)	4.8312E−5(5.67E−15)	3.6850E−3(1.48E−14)
	6	2.1542E−2(7.03E−16)	7.7069E−2(8.71E−16)	1.4377E−5(4.08E−14)	1.1604E−3(1.06E−13)
$\boldsymbol{\omega}^h$	2	4.7436E−2(6.76E−16)	5.1309E−2(9.59E−16)	2.8846E−4(1.22E−14)	1.2456E−2(3.17E−14)
	4	2.3986E−2(2.98E−15)	3.8150E−2(3.31E−15)	8.2990E−5(2.63E−13)	1.0417E−3(1.00E−12)
	6	1.6008E−2(2.10E−14)	2.2952E−2(2.25E−14)	3.0156E−5(4.08E−12)	2.3494E−4(1.02E−11)
$\boldsymbol{\sigma}^h$	2	9.3659E−1(1.84E−14)	2.6588(3.13E−14)	5.6919E−3(2.21E−13)	4.5920E−1(4.12E−13)
	4	4.5869E−1(8.16E−14)	1.6633(6.25E−14)	1.6879E−3(4.03E−12)	6.1945E−2(1.48E−11)
	6	3.0391E−1(2.58E−13)	1.1638(2.82E−13)	6.2626E−4(5.39E−11)	1.9624E−2(1.43E−10)

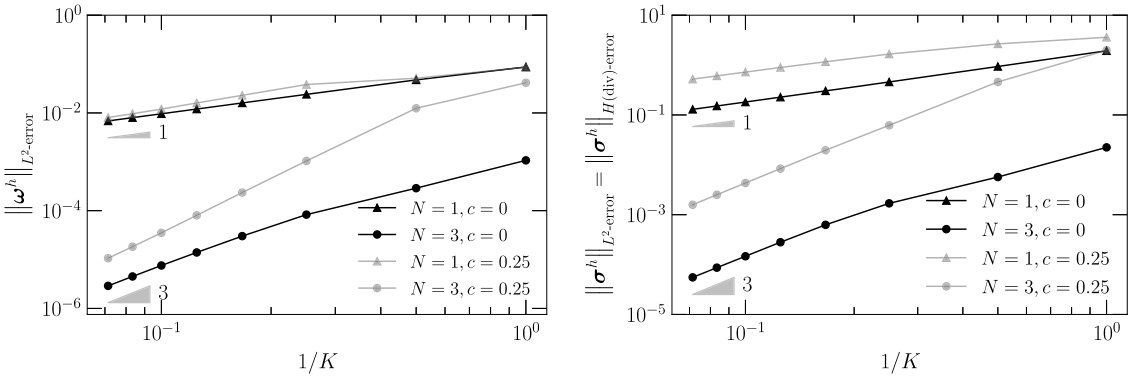

Fig. 6. The L^2-error of $\boldsymbol{\omega}^h$ (Left) and the $H(\text{div})$-error of $\boldsymbol{\sigma}^h$ (Right) for $N \in \{1, 3\}$, $K \in \{1, 2, 4, 6, \cdots, 14\}$, and $c \in \{0, 0.25\}$.

In Fig. 6, we present the results of the hMSEM for the L^2-error of the solution $\boldsymbol{\omega}^h$ and the $H(\text{div})$-error of the solution $\boldsymbol{\sigma}^h$, and in Fig. 7, we present the L^2-error and the H^1-error of the solution $\boldsymbol{u}^h$. It is seen that optimal convergence rates are obtained for solutions $\boldsymbol{\omega}^h$ and $\boldsymbol{u}^h$ with respect to the L^2-error and for the solution $\boldsymbol{\sigma}^h$ with respect to the $H(\text{div})$-error. These results are consistent with those of the MSEM [6]. As for the $\widetilde{H}^1$-error of the solution $\boldsymbol{u}^h$, we can see that it converges at the same rate as the L^2-error of the solution $\boldsymbol{u}^h$ does, which means it converges at a rate that is one order higher than the optimal order; superconvergence is obtained for $\boldsymbol{u}^h$. This is because, as we have explained in the last paragraph of Section 4.3.2, when we compute the $\widetilde{H}^1$-error of $\boldsymbol{u}^h$ the solution of its trace variable $\boldsymbol{\lambda}^h$ (as well as the given boundary condition $\widehat{\boldsymbol{u}}$) is used. These results show that the solution $\boldsymbol{\lambda}^h$ is correct.

The results for equilibrium of forces, $D\boldsymbol{\sigma}^h + \boldsymbol{f} = 0$ (in this case, $\boldsymbol{f} = \boldsymbol{f}^h = \boldsymbol{0}$), and equilibrium of moments, $R\boldsymbol{\sigma}^h = 0$, using the hMSEM are presented in Fig. 8. It is clear that equilibrium of forces is satisfied to the machine precision. The increase

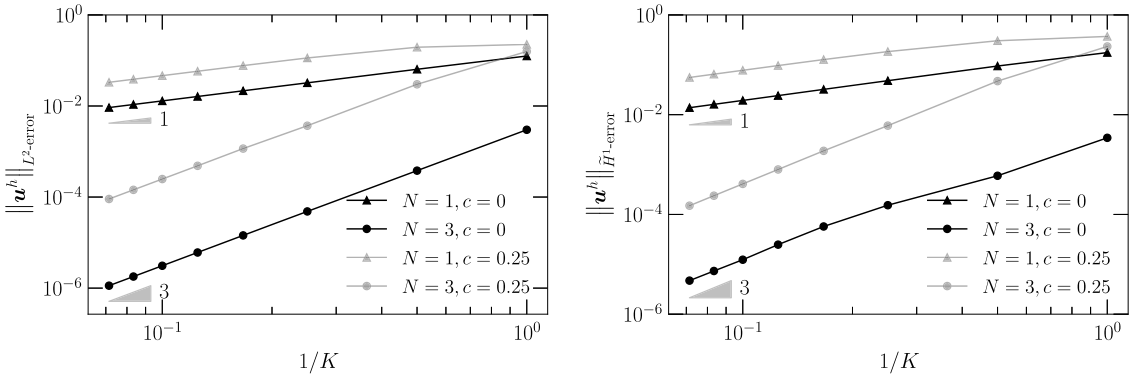

Fig. 7. The L^2-error (Left) and the $\widetilde{H}^1$-error (Right) of $\boldsymbol{u}^h$ for $N \in \{1, 3\}$, $K \in \{1, 2, 4, 6, \cdots, 14\}$, and $c \in \{0, 0.25\}$.

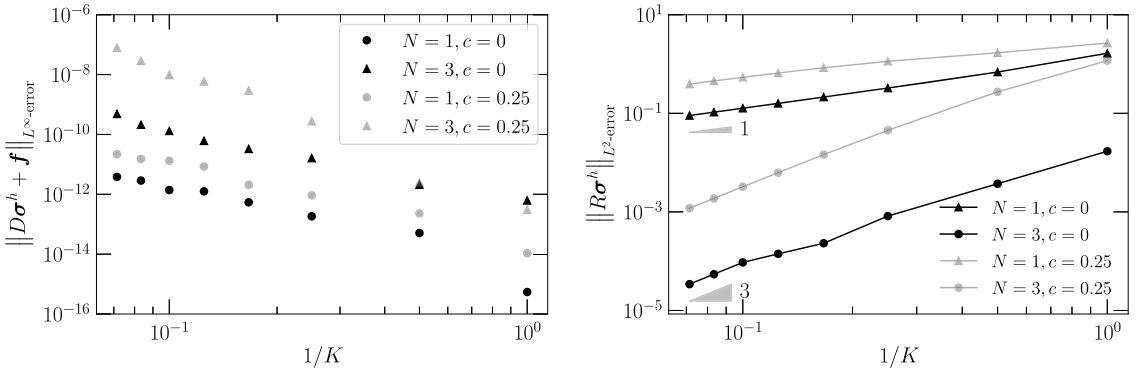

Fig. 8. The L^∞-error of $\left(D\boldsymbol{\sigma}^h + \boldsymbol{f}\right)$ (Left) and the L^2-error of $R\boldsymbol{\sigma}^h$ (Right) for $N \in \{1, 3\}$, $K \in \{1, 2, 4, 6, \cdots, 14\}$, and $c \in \{0, 0.25\}$.

of the L^∞-error of $\left(D\boldsymbol{\sigma}^h + \boldsymbol{f}\right)$ when we refine the mesh is because of the increasing accumulation of the machine error (a result of the rising of the total number of degrees of freedom and the increase in condition number). As for equilibrium of moments, it is only satisfied weakly; with the refinement of the mesh, the L^2-error of $R\boldsymbol{\sigma}^h$ converges at the optimal rate in both orthogonal and curvilinear meshes.

5.2.1. Cracked arch bridge

We test the hMSEM using a problem with a singularity. The geometry of the computational domain is shown in Fig. 9. It simulates an arch bridge which has a crack of depth $d = 0.25$ developing from the bridge bottom at the middle surface $y = 2$ where the minimal bridge thickness $D = 0.5$ is present. The bridge has a uniform body force field $\boldsymbol{f} = (1, 0, 0)$. The material properties E and ν are set to $E = 400$ and $\nu = 0.3$. The two walls $y = 0$ and $y = 4$ are considered as fixed walls. A load $\widehat{\boldsymbol{t}} = \left\{\widehat{\sigma}_{xx} \quad \widehat{\sigma}_{xy} \quad \widehat{\sigma}_{xz}\right\}^\mathsf{T} = \left\{\widehat{\sigma}_{xx} \quad 0 \quad 0\right\}^\mathsf{T}$, where

$$\widehat{\sigma}_{xx} = -\sin(\frac{\pi y}{4})e^{-(y-2)^2},$$

is applied on the bridge floor $(x, y, z) \in 0 \times (0, 2) \times (0, 1)$. All remaining walls are considered as zero-surface-traction walls. These boundary conditions will tend to open the crack and therefore introduce a singularity in the solution σ^h_{yy} at the crack root: For $x = 0.25^-$, σ^h_{yy} will increase to extremely large value, but it has to return to the designed value, $\sigma^h_{yy} = 0$, for $x = 0.25^+$. This singularity makes this problem a challenging one. However, since the hMSEM (as well as the MSEM) places no degree of freedom at edges and corners of the elements, it needs no special treatment to handle this singularity. The polynomial degree is set to $N_\xi = N_\eta = N_\varsigma = N$. A mesh of 780 elements is generated using transfinite interpolation [45,46], and a local refinement is made near the singularity. The solution of σ^h_{yy} for $N = 1$ in Fig. 11 can reveal the local refinement along x-axis.

In Fig. 10, representative results of the Von Mises stress for $N = 4$ are shown. It is seen that near the singularity some unphysical oscillations are present. This is because of the complexity of the singularity and, as we use a direct linear solver, the mesh used in this work is not extremely refined. More local refinement near the singularity will weaken such oscillations. In Fig. 11, the results of σ^h_{yy} along $(x, y, z) \in (0, 0.5) \times 2 \times 0.5$ for $N = 1, 2, 3, 4$ are presented. It is seen that σ^h_{yy} is discontinuous across elements along x-axis, which is consistent with the fact that only the surface tractions across

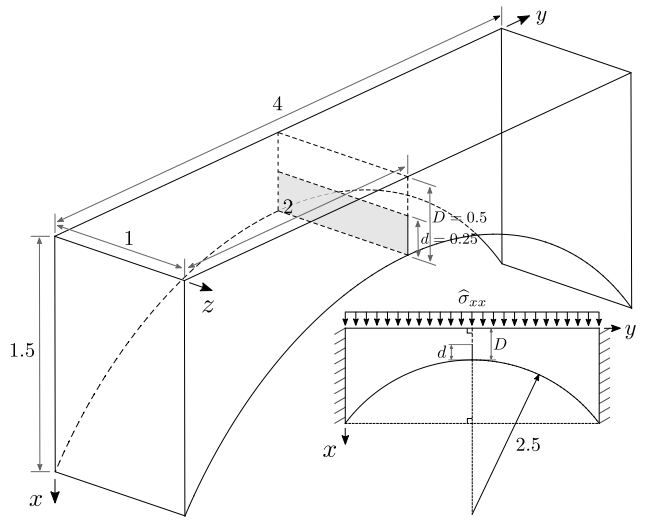

Fig. 9. The geometry of the cracked arch bridge. The gray surface indicates the rectangular crack.

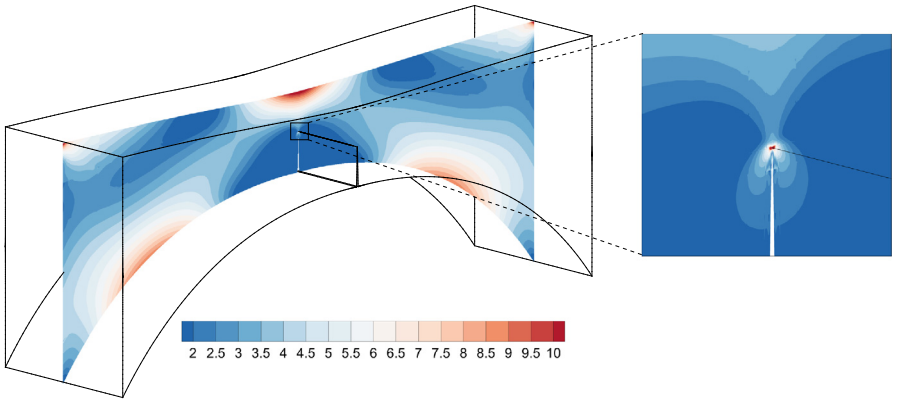

Fig. 10. The deformation plot of the Von Mises stress on surface $z = 0.5$ for $N = 4$.

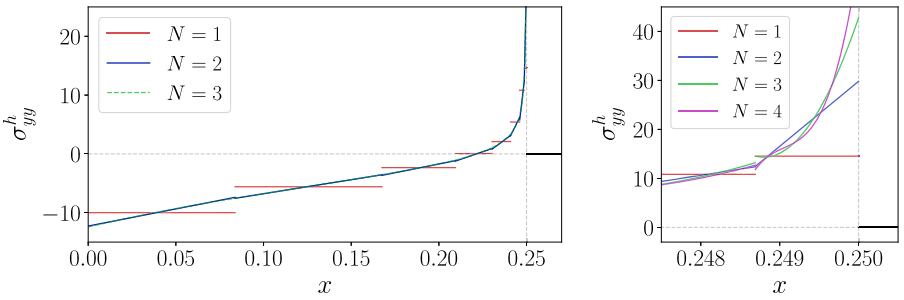

Fig. 11. Results of solution σ^h_{yy} along $(x, y, z) \in (0, 0.25^+) \times 2 \times 0.5$ for $N \in \{1, 2, 3, 4\}$.

elements along the outward normal direction are enforced to be continuous by the Lagrange multiplier. It is also seen that the singularity in σ^h_{yy} is well captured with this method.

The results of the complementary energy, see (3), and the resultant crack width are shown in Table 4. The crack width is measured at $(x, y, z) = (0.5, 2, 0.5)$.

6. Conclusions

In this paper, we have proposed a hybrid mimetic spectral element method that solves three-dimensional linear elasticity problems. It decomposes the domain into discontinuous elements (subdomains) and has the potential to lower the computational cost significantly compared to the existing mimetic spectral element method. Optimal convergence rates are

Table 4
Results of the complementary energy CE and the resultant crack width w_c.

	$N=1$	$N=2$	$N=3$	$N=4$
CE	6.9592E−02	6.8854E−02	6.8771E−02	6.8747E−02
w_c	1.1392E−02	1.2987E−02	1.2968E−02	1.2968E−02

observed for the displacement and rotation solutions with respect to their L^2-error and for the stress solution with respect to its $H(\mathrm{div})$-error, and superconvergence is observed for the displacement solution with respect to its $\widetilde{H}^1$-error. The method is free of spurious kinematic modes and satisfies pointwise equilibrium of forces in all meshes, orthogonal or curvilinear, coarse or refined.

CRediT authorship contribution statement

Yi Zhang: Conceptualization, Methodology, Software, Validation, Writing – Original Draft, Writing – Review & Editing, Visualization, Revision. **Joël Fisser:** Methodology, Investigation, Writing – Review & Editing, Revision. **Marc Gerritsma:** Supervision, Conceptualization, Methodology, Writing – Review & Editing, Revision.

Declaration of competing interest

The authors declare that they have no known competing financial interests or personal relationships that could have appeared to influence the work reported in this paper.

Acknowledgements

The research of Yi Zhang is supported by the China Scholarship Council under grant number 201607720010. We also thank the reviewers for their valuable contributions.

References

[1] M. Gerritsma, An introduction to a compatible spectral discretization method, Mech. Adv. Mat. Struct. 19 (1–3) (2012) 48–67.
[2] J. Kreeft, M. Gerritsma, Mixed mimetic spectral element method for Stokes flow: a pointwise divergence-free solution, J. Comput. Phys. 240 (2013) 284–309.
[3] A. Palha, P.P. Rebelo, R. Hiemstra, J. Kreeft, M. Gerritsma, Physics-compatible discretization techniques on single and dual grids, with application to the Poisson equation of volume forms, J. Comput. Phys. 257 (2014) 1394–1422.
[4] A. Palha, B. Koren, F. Felici, A mimetic spectral element solver for the Grad–Shafranov equation, J. Comput. Phys. 316 (2016) 63–93.
[5] D. Lee, A. Palha, M. Gerritsma, Discrete conservation properties for shallow water flows using mixed mimetic spectral elements, J. Comput. Phys. 357 (2018) 282–304.
[6] K. Olesen, B. Gervang, J.N. Reddy, M. Gerritsma, A higher-order equilibrium finite element method, Int. J. Numer. Methods Eng. 114 (2018) 1262–1290.
[7] T.H. Pian, C.-C. Wu, Hybrid and Incompatible Finite Element Methods, Chapman and Hall/CRC, 2005.
[8] F. Brezzi, M. Fortin, Mixed and Hybrid Finite Element Methods, vol. 15, Springer Science & Business Media, 2012.
[9] K. Lipnikov, G. Manzini, M. Shashkov, Mimetic finite difference method, J. Comput. Phys. 257 (2014) 1163–1227.
[10] L. Beirão da Veiga, F. Brezzi, A. Cangiani, G. Manzini, L.D. Marini, A. Russo, Basic principles of virtual element methods, Math. Models Methods Appl. Sci. 23 (01) (2013) 199–214.
[11] A.L. Gain, C. Talischi, G.H. Paulino, On the virtual element method for three-dimensional linear elasticity problems on arbitrary polyhedral meshes, Comput. Methods Appl. Mech. Eng. 282 (2014) 132–160.
[12] E. Tonti, The algebraic-topological structure of physical theories, Symmetry, Similarity Group Theor. Meth. Mech. (1974) 441–467.
[13] E. Tonti, The Mathematical Structure of Classical and Relativistic Physics, Springer, 2013.
[14] A. Bossavit, On the geometry of electromagnetism, Jpn. Soc. Appl. Electromagn. Mech. 6 (1998) 17–28, 114–123, 233–240, 318–326.
[15] P.B. Bochev, J.M. Hyman, Principles of Mimetic Discretizations of Differential Operators, in: Compatible Spatial Discretizations, Springer, 2006, pp. 89–119.
[16] D.N. Arnold, R.S. Falk, R. Winther, Finite element exterior calculus, homological techniques, and applications, Acta Numer. 15 (2006) 1–155.
[17] D.N. Arnold, R.S. Falk, R. Winther, Finite element exterior calculus: from Hodge theory to numerical stability, Bull. Am. Math. Soc. 47 (2) (2010) 281–354, arXiv:0906.4325.
[18] E. Tonti, Why starting from differential equations for computational physics?, J. Comput. Phys. 257 (2014) 1260–1290.
[19] T.H. Pian, Derivation of element stiffness matrices by assumed stress distributions, AIAA J. 2 (7) (1964) 1333–1336.
[20] P. Tong, New displacement hybrid finite element models for solid continua, Int. J. Numer. Methods Eng. 2 (1) (1970) 73–83.
[21] T.H. Pian, Variational principles for incremental finite element methods, J. Franklin Inst. 302 (5–6) (1976) 473–488.
[22] F. Ben Belgacem, Y. Maday, The mortar element method for three dimensional finite elements, ESAIM: Math. Model. Numer. Anal. 31 (2) (1997) 289–302.
[23] F. Ben Belgacem, The mortar finite element method with Lagrange multipliers, Numer. Math. 84 (2) (1999) 173–197.
[24] B.I. Wohlmuth, A mortar finite element method using dual spaces for the Lagrange multiplier, SIAM J. Numer. Anal. 38 (3) (2000) 989–1012.
[25] C. Farhat, F.-X. Roux, A method of finite element tearing and interconnecting and its parallel solution algorithm, Int. J. Numer. Methods Eng. 32 (6) (1991) 1205–1227.
[26] A. Klawonn, O.B. Widlund, Dual-primal FETI methods for linear elasticity, Commun. Pure Appl. Math.: A Journal Issued by the Courant Institute of Mathematical Sciences 59 (11) (2006) 1523–1572.
[27] J.M. de Almeida, E.A. Maunder, Equilibrium Finite Element Formulations, Wiley Online Library, 2017.
[28] M. Kempeneers, J.-F. Debongnie, P. Beckers, Pure equilibrium tetrahedral finite elements for global error estimation by dual analysis, Int. J. Numer. Methods Eng. 81 (4) (2010) 513–536.

[29] L. Wang, H. Zhong, A traction-based equilibrium finite element free from spurious kinematic modes for linear elasticity problems, Int. J. Numer. Methods Eng. 99 (10) (2014) 763–788.
[30] F. Brezzi, On the existence, uniqueness and approximation of saddle-point problems arising from Lagrangian multipliers, Publ. Math. Inf. Rennes (S4) (1974) 1–26.
[31] D.N. Arnold, F. Brezzi, Mixed and nonconforming finite element methods: implementation, postprocessing and error estimates, ESAIM: Math. Model. Numer. Anal. 19 (1) (1985) 7–32.
[32] P. Woźny, Construction of dual bases, J. Comput. Appl. Math. 245 (2013) 75–85.
[33] P. Woźny, Construction of dual B-spline functions, J. Comput. Appl. Math. 260 (2014) 301–311.
[34] V. Jain, Y. Zhang, A. Palha, M. Gerritsma, Construction and application of algebraic dual polynomial representations for finite element methods on quadrilateral and hexahedral meshes, Comput. Math. Appl. (2020).
[35] C. Carstensen, L. Demkowicz, J. Gopalakrishnan, Breaking spaces and forms for the DPG method and applications including Maxwell equations, Comput. Math. Appl. 72 (3) (2016) 494–522.
[36] M. Gerritsma, Edge functions for spectral element methods, Spectr. High Order Meth. Partial Differ Equ. (2011) 199–207.
[37] M. Gerritsma, A. Palha, V. Jain, Y. Zhang, Mimetic spectral element method for anisotropic diffusion, in: D. Di Pietro, A. Ern, L. Formaggia (Eds.), Numerical Methods for PDEs, in: SEMA SIMAI Springer Series, Cham, 2018, pp. 283–301.
[38] Y. Zhang, V. Jain, A. Palha, M. Gerritsma, The discrete Steklov–Poincaré operator using algebraic dual polynomials, Comput. Methods Appl. Math. 19 (3) (2019) 645–661.
[39] A. Buffa, J. Rivas, G. Sangalli, R. Vázquez, Isogeometric discrete differential forms in three dimensions, SIAM J. Numer. Anal. 49 (2) (2011) 818–844.
[40] J.A. Evans, Divergence-free B-spline discretizations for viscous incompressible flows, Ph.D. thesis, 2011.
[41] W. Dornisch, J. Stöckler, R. Müller, Dual and approximate dual basis functions for B-splines and NURBS–comparison and application for an efficient coupling of patches with the isogeometric mortar method, Comput. Methods Appl. Mech. Eng. 316 (2017) 449–496.
[42] D. Boffi, F. Brezzi, M. Fortin, et al., Mixed Finite Element Methods and Applications, vol. 44, Springer, 2013.
[43] A. Quarteroni, A. Valli, Theory and Application of Steklov-Poincaré Operators for Boundary-Value Problems, Applied and Industrial Mathematics, Dordrecht, 1991.
[44] J. Mandel, R. Tezaur, Convergence of a substructuring method with Lagrange multipliers, Numer. Math. 73 (4) (1996) 473–487.
[45] W.J. Gordon, C.A. Hall, Transfinite element methods: Blending-function interpolation over arbitrary curved element domains, Numer. Math. 21 (2) (1973) 109–129.
[46] S. Steinberg, Fundamentals of Grid Generation, CRC Press, 1993.